Sustainable Energy & Fuels

ROYAL SOCIETY OF CHEMISTRY

PAPER

View Article Online
View Journal | View Issue

Cite this: *Sustainable Energy Fuels*, 2022, **6**, 5474

Probing elemental speciation in hydrochar produced from hydrothermal liquefaction of anaerobic digestates using quantitative X-ray diffraction†

Hanifrahmawan Sudibyo *[ab] and Jefferson W. Tester [a]

Valorization of hydrochar, a solid byproduct from hydrothermal liquefaction (HTL) of anaerobically-digested agriculture wastes (digestates), requires fundamental knowledge of elemental speciation. This study investigated the effects of reaction temperatures (320–360 °C), digestate pH (3.5–8), and digestate cellulose-to-lignin ratios (0.2–1.8) on the speciation (chemical form) and composition of organics and inorganics in hydrochars produced during hydrothermal treatment. Quantitative X-ray diffraction (XRD) method was the primary technique used to characterize hydrochars. The comprehensive XRD pattern processing including the Rietveld refinement protocols demonstrated that the organic phase was comprised of mostly crystalline monocyclic, heterocyclic, and polycyclic aromatics with diverse aliphatic and aromatic substituents, while the inorganic mineral phase consisted of calcium-phosphates, magnesium-phosphates, calcium-carbonates, and magnesium-carbonates. XRD results were validated by the elemental yields of products and the distribution of chemical functionalities measured using solid-state nuclear magnetic resonance (NMR) spectroscopy. The characterization data were used to evaluate proposed mechanistic pathways using compositional analysis of biocrude and aqueous-phase coproducts. Mechanistic pathways developed in the study suggested that benzoic acids, phenols, benzaldehydes, phenolic aldehydes, α-dicarbonyls, and α-hydroxycarbonyls were responsible for the precipitation of organics through various reactions depending on operating conditions. Meanwhile, the formation of inorganic compounds appeared to be consistently represented by reactions including dehydration, hydrolysis, endergonic reduction, and structure rearrangement of native minerals in the digestates. This study provides basic knowledge needed to create and assess potential elemental speciation pathways. In addition, the results of the study facilitate the specification of process conditions to optimize targeted utilization routes of hydrochar for more economically-feasible and sustainable HTL processing.

Received 6th August 2022
Accepted 28th October 2022

DOI: 10.1039/d2se01092e

rsc.li/sustainable-energy

1 Introduction

Resource recovery from anaerobic digestates using hydrothermal liquefaction can effectively mitigate potential environmental pollution caused by direct land spreading of the digestates on farms and pastures for soil amendment or fertilizer, *e.g.*, residual greenhouse gases emissions, water basin eutrophication and acidification due to excessive runoff of nutrients into river basins and lakes, and cross-contamination between farm and food production facility.[1] Hydrothermal liquefaction (HTL) processing at 280 to 360 °C and 10 to 20 MPa convert lignocellulosic carbon and nutrients contained in the digestates produced during anaerobic digestion into renewable biocrude oil and a nutrient-rich aqueous-phase (HTL-AP) coproduct that can be further processed for (NPK) recovery using a number of methods including struvite crystallization,[2] ammonia stripping,[3] and membrane separation.[4] In addition, HTL produces a solid carbonaceous coproduct called hydrochar with relatively similar carbon and energy content to brown coal (lignite) and comparable nutrient content to low-grade phosphate rock.[5]

Hydrochar formation is considered disadvantageous from HTL operational perspective since it can adsorb 55–80% of the total biocrude oil produced,[2,6] leading to a requirement of filtration followed by extraction using non-polar organic solvent to recover the biocrude. Because the addition of these two processes increases the HTL operational cost, efforts have been made to suppress hydrochar formation during HTL. The

[a]*School of Chemical and Biomolecular Engineering, Energy Systems Institute, Cornell University, Ithaca, New York 14853, USA. E-mail: hs987@cornell.edu*

[b]*Chemical Engineering Department, Universitas Gadjah Mada, Yogyakarta 55281, Indonesia*

† Electronic supplementary information (ESI) available. See DOI: https://doi.org/10.1039/d2se01092e

experimental-based optimization of the process parameters (*e.g.*, reaction temperature and time, pH of reaction mixture, and solid heterogeneous catalyst concentration) based on the feedstock compositions (*e.g.*, moisture content and composition of lignin, cellulose, protein, lipid, and minerals) has been performed over various wet biomass waste using response surface[7–10] and mixture design (*i.e.*, simplex centroid,[10] simplex lattice,[11] and extreme vertices[12]) protocols. Nevertheless, the minimized hydrochar yield is still relatively high between 5–45%, which means that the hydrochar formation is inevitable and thus, the filtration and extraction are still required. Valorization of hydrochar into marketable products is critical to adequately compensate for the extra costs associated with these two processes.

Traditional valorization routes for hydrochar include using it as solid fuel, soil amendment/fertilizer, and/or water pollutant adsorbent,[13] while more advanced routes include utilization as immobilization media for bioprocess,[14] catalyst and catalyst support,[15] electrochemical supercapacitor electrode material,[16] and carbon quantum dot precursor.[17] Determining the best valorization route depends on the physical, thermal, and chemical properties of the hydrochar. These properties are associated with the composition and speciation (chemical form) of elements, which are greatly affected by the HTL process conditions and feedstock compositions.[18–21]

Several analytical techniques have been reported in the literature to help understand how these factors affect the fate of elements in the hydrochar. The ASTM D5373-21 procedure[22] using a high-temperature combustion–reduction instrument is performed to measure C, H, O, and N content of hydrochar, which is subsequently used to calculate the elemental yield. Similarly, the yield of inorganic nutrient in the hydrochar can be calculated based on the elemental content measurement using a colorimeter[20] or a spectrometry instrument, *i.e.*, inductively coupled plasma with mass spectrometer (ICP-MS) or optical emission spectrometer (ICP-OES),[23] X-ray fluorescence (XRF) spectrometer,[24] and energy-dispersive X-ray (EDX) spectrometer.[25]

While the analytical techniques to measure the elemental composition are well-established, more efforts are required to improve the characterization of the elemental speciation. Spectroscopy techniques with Fourier transform infra-red (FTIR), X-ray photoelectron (XPS), and the ^{13}C, ^{1}H, and ^{31}P solid-state nuclear magnetic resonance (SS-NMR) are usually employed to observe the profile of chemical functionalities in the hydrochar.[26–28] However, FTIR methods suffer from overlapping peaks representing different functional groups, and XPS requires high vacuum environment and can only detect functional groups of elements with atomic number ≥ 3, *i.e.*, cannot detect carbon–hydrogen bond. Although the recently developed SS-NMR techniques (*i.e.*, cross- or direct-polarization magic-angle spinning combined with dipolar dephasing, ^{13}C chemical-shift-anisotropy filter, 2D heteronuclear correlation, and long-range recoupled H–C dipolar dephasing)[27–29] allow to quantify the distribution of C, H, and P based on their corresponding chemical bonds, they still cannot inform the complete chemical structure and mass composition of constituent compounds of hydrochar. In addition, the detection of carbon–nitrogen bonding using SS-NMR is limited by the requirement of isotopic labeling of nitrogen as ^{15}N.

X-ray diffraction (XRD) can be used in parallel to the aforementioned techniques to identify and quantify the chemical composition of solid mixtures based on the summation of different diffraction patterns resulting from the molecular structure of all constituent compounds.[30] Recent use of XRD for hydrochar characterization, however, has been limited to qualitative analysis, *i.e.*, to identify mineral phases and determine the degree of crystallinity.[28,31] With massive expansion of diffraction pattern database by the International Centre For Diffraction Data (ICDD) for amorphous/crystalline organic and inorganic compounds (*e.g.*, PDF-4/minerals, PDF-4/organics, and PDF-4/inorganics)[32] and the advanced development of algorithm of diffraction pattern processing particularly for the whole pattern-based quantification (*e.g.*, BGMN, TOPAS, and JADE),[33] the use of XRD can be upgraded to analyze the speciation of not only the minerals but also organic phase of hydrochar's constituents quantitatively.

Characterizing elemental speciation is critical to determine sustainable valorization routes for hydrochar. Specifically, elemental speciation provides specific chemical structures and concentrations of corresponding chemical species in the material. This information is required to evaluate the physicochemical, electrochemical, and biological properties of hydrochar including its toxicity, mobility, bioavailability, and lifetime, fate, and degradability.[34] For instance, hydrochar containing water-soluble minerals such as monetite ($CaHPO_4 \cdot 2H_2O$) and struvite ($MgNH_4PO_4 \cdot 6H_2O$) can provide a higher bioavailability of P for plants than hydrochars containing less-water-soluble minerals such as hydroxyapatite ($Ca_{10}(PO_4)_6(OH)_2$),[35] even though they have similar P content. Likewise, if hydrochar is to be used as soil amendment/fertilizer, speciation of carbon and nitrogen as aromatic carboxylic acids (*e.g.*, humic acid and fulvic acid) and aliphatic amides (*e.g.*, urea) is preferred. For example, from an ecotoxicological standpoint aromatic carboxylic acids have lower negative impacts than polycyclic aromatics, *O*-heterocyclics, and *N*-heterocyclics on plant's growth and development,[36] regardless of the carbon and nitrogen content. In contrast, having the organic carbon in the form of *O*-heterocyclics and *N*-heterocyclics in the hydrochar is required for manufacturing hydrochar-based carbon nanotubes with high-performance supercapacitance.[37,38]

For process optimization, understanding the elemental speciation in hydrochar aids in selecting operating conditions to obtain hydrochar with properties suitable for more sustainable application. However, previous studies of the chemistry of elemental speciation in hydrochar is limited to HTL systems processing only cellulose or lignin as the feedstock at a narrow range of operating conditions. Shi *et al.*[39] suggested that furans are the precursors of hydrochar formation during non-catalytic hydrothermal conversion of cellulose at 250 °C through a series of steps including hydrolytic furanic-ring opening, aldol condensation, acetal cyclization, and etherification. Sturgeon *et al.*[40] and Schutyser *et al.*[41] discovered that phenyloxiranes

(epoxides), Hibbert's ketones, and quinone methides are the precursors of hydrochar formation during acid-catalyzed hydrothermal processing of lignin at 300 °C through several repolymerization mechanisms. Unfortunately, these studies proposed ideas regarding hydrochar precursors by characterizing only the hydrochar without analyzing the composition of chemical substances in the other product phases. Consequently, the proposed mechanisms may only represent a partial information on chemistry of hydrochar formation. Moreover, the findings of these studies are not applicable to HTL systems operating at much higher temperature, employing acidic or alkaline catalysis, and processing feedstocks containing a mixture of organic and inorganic matrices, particularly when cellulose and lignin are mixed and coexist with nitrogenous compounds (*e.g.*, protein, amino acids, and ammonia) and inorganics in the feedstocks. While Leng and coworkers in their review paper have proposed melanoidins and Mannich bases produced by Maillard and Mannich reactions, respectively, as precursors of hydrochar formation in the HTL of nitrogen-rich lignocellulosic feedstocks,[42] these proposed mechanisms are hypothetical and requires further investigations.

Similarly, previous studies of the speciation of inorganics in hydrochar have only focused on the transformation of P during HTL of wet biomass wastes and have always assumed that P precipitates in hydrochar through the formation of apatite[20,43] (*e.g.*, hydroxyapatite) and non-apatite inorganic phosphate minerals, *e.g.*, vivianite, varulite, and strunzite.[44,45] These studies did not comprehensively assess the profile of P speciation in the aqueous phase (*e.g.*, *via* functional group identification with ^{31}P NMR), ignoring the possibility of P precipitation by chemically bonding aqueous aromatics that are susceptible to repolymerization into hydrochar during HTL.

The limitations of these earlier investigations motivated our study to evaluate how reaction conditions affect the mechanism of hydrochar formation. Specifically, we examined how HTL reaction temperature, acid and alkaline catalysis, and feedstock cellulose-to-lignin ratio affect elemental speciation in the hydrochar during HTL of ammonia-rich anaerobic digestates. To achieve this goal, we evaluated the chemical evolution of all the HTL product phases. The evolution of elemental speciation and the chemical species composition in hydrochar were characterized using the quantitative XRD technique. The quantification follows the whole pattern fitting (WPF) and Rietveld refinement protocols for full diffraction pattern processing.[46,47] To validate the quantitative XRD results, (1) the elemental balances were calculated based on the measured mass yield and elemental content of all the product phases and (2) the distribution of chemical functionalities of hydrochar were measured using the direct polarization magic-angle spinning (DP-MAS) SS-NMR spectroscopy of ^{13}C, ^{31}P, ^{43}Ca, and ^{25}Mg. Subsequently, the liquid-state ^{13}C and ^{31}P NMR analysis of the biocrude and HTL-AP were performed to characterize the composition of the organic compounds and the distribution of phosphorus functional groups. The obtained biocrude and HTL-AP compositions together with the chemical species composition of hydrochar were used to develop multiphase reaction mechanisms associated with the elemental speciation in the hydrochar. To accomplish this, we combined theoretical chemistry predictions with thermodynamic assessment of the potential reactions using a heuristic graph-based approach.

2 Materials and methods

2.1 Feedstock preparation

The model anaerobic digestates were synthetically prepared by mixing specific representative compounds with 200 mL ultrapure water (18.2 mΩ·cm) to control the feedstock cellulose-to-lignin ratio and pH. Organic fractions were represented by alkaline lignin (≥94%, SCBT), microcrystalline cellulose (≥99.99%, MilliporeSigma), glutamic acid (≥99.99%, BioBasic), and NH_4-acetate (≥99.99%, J.T. Baker). Inorganic fractions were represented by $CaHPO_4{\cdot}2H_2O$ (≥99%, Eisen-Golden), $CaCO_3$ (≥99%, Loudwolf), $MgCO_3$ (≥98%, Aldon Corp.), and KCl (≥99.99%, EMD Chemicals). The rationale for the selection of these compounds was explained in an earlier study.[2]

In the model digestate mixture, the total content of alkaline lignin and microcrystalline cellulose was maintained at 8 wt%,[48] the total content of glutamic acid and ammonium-acetate was kept constant at 3 wt% (with NH_3–N to organic–N molar ratio of 3 : 1),[49] and the inorganic content was fixed at 5 wt% (equivalent to 31% ash content on dry matter basis).[48] The cellulose-to-lignin ratio was varied between 0.2–1.8 according to the reported values in the literature for anaerobic digestate.[48] The content of the inorganics, which are $CaHPO_4{\cdot}2H_2O$, $CaCO_3$, $MgCO_3$, and KCl were fixed at 1.25, 0.72, 1.41, and 1.62 wt%, respectively, to provide K : Ca : Mg : P molar ratio of 3 : 2 : 2 : 1.[50] The mixture pH was adjusted to pH 3.5 and 8 by adding acetic acid (≥99.5%, J.T. Baker) and NaOH (≥99.99%, Belle Chemical), respectively. A pH 3.5 was selected because it maximizes biocrude formation and nutrient yield in HTL-AP, inhibits *N*-fixation in biocrude, and suppresses hydrochar formation,[2] while pH 8 was selected as it represents typical digestate pH that range from 7.5 to 8.5.[48]

2.2 HTL procedures and yield calculations

Triplicate HTL experiments over synthetic anaerobic digestates with different cellulose-to-lignin ratios (0.2 and 1.8) and pH (3.5 and 8) were carried out at 320–360 °C and 50 min. The reaction temperatures of 320–360 °C were selected because they allow higher energy recovery by promoting deoxygenation and denitrogenation of biocrude product phase during the HTL of digestates.[2] The reaction time of 50 min was selected based on the optimal value for complete decomposition of cellulose and lignin.[2] The experimental setup and procedures were similar to those described in our previous study[8] (see Fig. S1†). From each set of experiment, the collected products were (1) biocrude oil, which is a mixture of three biocrude extraction fractions, *i.e.*, dichloromethane- and ethyl-acetate-extracted water-soluble biocrudes and dichloromethane-extracted solid-bound biocrude; (2) solid hydrochar; and (3) aqueous-phase coproduct (HTL-AP).

The C, H, O, and N content of biocrude and hydrochar were measured by combustion (980 °C) and reduction (650 °C) using

Exeter Analytical CE-440 CHN/O Analyzer. The total concentrations of organic carbon and nitrogen in HTL-AP were measured by catalytic oxidation at 720 °C using an integrated Shimadzu TOC-L and TNM-L modules, which employs an infrared and a chemiluminescence detector, respectively. The content of inorganic elements in the hydrochar was measured using Oxford Instruments EDX spectrometer (with AZtecLive and Ultim Max detector) integrated with Zeiss Gemini 500 SEM. The SEM-EDX operating parameters are the following: electron beam of 20 keV, working distance of 8 mm, lens aperture size of 60 μm, InLens detector, resolution of 1024 pixels, process time of 6, and acquisition time of 120 s. The aqueous concentration of P, Ca, and Mg were determined following the vanadomolybdophosphoric acid,[51] oxalate,[52] and calmagite[53] methods, respectively, by means of Hanna Instrument HI83399 photometer. The calculation steps for mass yield of products and elements are given in Table S1 in the ESI.†

2.3 Quantitative XRD analysis

The hydrochar samples were finely ground using Fritsch Pulverisette 7 ball mill and separated by the dry sieve method using ATM Sonic Sifter Model L3P with a 635-mesh screen to obtain ultra-fine particle size ≤20 micron. The ultra-fine particle size allows high-resolution measurement and high-accuracy Rietveld refinement. The XRD pattern was acquired at room temperature over 2θ range of 10–80° with a step size of 0.01° using Bruker D8 Advance ECO diffractometer (1 kW/40 kV/25 mA, Cu K_α radiation at 1.5406 Å). The divergent beam slit, detector slit, and position sensitive detector opening were set at 0.6 mm, 9 mm, and 2.747 mm, respectively.

The obtained XRD pattern was processed on MDI Jade 7.8.2 to measure the degree of crystallinity and quantify the organic and mineral phase compositions based on the PDF-4/organics and PDF-4/minerals database.[32] The quantification following WPF and Rietveld refinement was carried out by minimizing the weighted residual variance (R_{WP}, see eqn (1)) between the measured and calculated intensities at each point (*i.e.*, the 2θ step) in the pattern. The minimization aimed to reach the expected R_{WP} value ($R_{WP,expected}$) calculated using eqn (2).

$$R_{WP} = \left(\frac{\sum_{j=1}^{j=N} w_j \left(I_{cal,j} - I_{obs,j}\right)^2}{\sum_{j=1}^{j=N} w_j \left(I_{obs,j}\right)^2} \right)^{0.5} \quad (1)$$

$$R_{WP,expected} = \left(\frac{N}{\sum_{j=1}^{j=N} w_j \left(I_{obs,j}\right)^2} \right)^{0.5} \quad (2)$$

where w_j is the weight assigned to the jth step intensity, $I_{cal,j}$ and $I_{obs,j}$ are the calculated and observed intensities at step j, respectively, and N is the total number of 2θ steps.

The R_{WP} minimization involved the adjustment of parameters used to calculate $I_{cal,j}$ in eqn (3). This equation considers (1) the possibility of more than one phase and more than one diffraction peak at a position 2θ; (2) the integral intensity of diffraction peaks including the overlapping peaks by using a more reliable profile shape function, *i.e.*, pseudo-Voigt function; and (3) the correction of preferred orientation using the March–Dollase function.[46]

$$I_{cal,j} = I_{BG,j} + \sum_a \left(S_a \sum_b M_{ab} L_{ab} F_{ab} G_{ab} P_{ab} \right) \quad (3)$$

where $I_{BG,j}$ is the refined background intensities, subscripts a and b indicates phase and its Miller indices (hkl) for the Bragg reflection, respectively, and S, M, L, F, G, and P are the phase-specific scale factor, multiplicity factor, Lorentz and polarization factor, pseudo-Voigt function,[46] and March–Dollase orientation function,[54] respectively.

Once the lowest R_{WP} value was reached, the weight fraction of mineral or organic phase a (w_a) in the n-phase mixture was calculated using eqn (4) based on the refined phase scale factor (S) and the unit cell mass (Z_M) and volume (V) determined by minimizing the Bragg residual (R_{Bragg}). The R_{Bragg} is the reflection intensity-based R-factor computed based on the contributing reflections of the estimated structure factors of each phase toward the calculated diffraction pattern. Ultimately, the obtained weight fractions were validated by comparing the XRD-predicted and measured elemental compositions of hydrochar.

$$w_a = S_a (Z_M)_a V_a \sum_{j=1}^{j=N} S_j (Z_M)_j V_j \quad (4)$$

2.4 NMR analysis

2.4.1 Solid-state NMR of hydrochar. The DP-MAS SS-NMR of ^{13}C, ^{31}P, ^{43}Ca, and ^{25}Mg were performed using a 500 MHz Bruker Avance II NMR spectrometer, with a 4 mm triple resonance probe and operating frequencies of 200, 125, 34, and 55 MHz for ^{13}C, ^{31}P, ^{43}Ca, and ^{25}Mg, respectively. Proton-decoupling techniques were employed to achieve high spectral resolution with high signal-to-noise ratio, narrower singlets, and less spectral overlap: (1) two-pulse phase-modulated proton-decoupling for ^{13}C, (2) continuous heteronuclear decoupling (^{31}P–^{1}H) on ^{1}H channel for ^{31}P, (3) spinal-64 ^{1}H decoupling for ^{43}Ca, and (4) continuous-wave proton decoupling for ^{25}Mg. Detailed operating conditions including the 90° pulse length, recycle delay, MAS rate, transient number, and reference compounds are given in Table S2 of the ESI.†

The acquired ^{13}C, ^{31}P, ^{43}Ca, and ^{25}Mg SS-NMR spectra of hydrochar were divided into seven, four, five, and three regions of chemical shift range, respectively, according to the functional group classification in the literature.[27,55–57] Each region excluding the peaks of solvent and internal standard was integrated and normalized to the total spectral area using MNova 14.2.3 (Mestrelab Research) to obtain the relative region area percentages, which correspond to the functionalities distribution. The integration results were validated by comparing the elemental content of hydrochar estimated based on the total spectral peak area (see eqn (5)) with that was directly measured

following the procedures in subsection 2.2. Moreover, the validation was performed by comparing the NMR-based and experimental-based (%$Z_{contributed}$, see eqn (6)) values for percent contribution of P, Mg, and Ca by the detected minerals toward the total content of these elements in the hydrochar.

$$\%\, E_{est,k} = \frac{I_k}{I_{std}} \times \frac{W_{std}}{W_k} \times \%\, E_{std} \quad (5)$$

$$\%\, Z_{contributed} = \frac{w_{mineral} \times \%\, Z_{mineral}}{\%\, Z_{HC}} \times 100\% \quad (6)$$

where % E, I, and W are the elemental content, spectral area, and mass (mg), respectively. The subscripts est, std, and k indicate NMR-based estimation, internal standard, and HTL product phase (*i.e.*, biocrude, hydrochar, and HTL-AP), respectively. The $w_{mineral}$, % $Z_{mineral}$, % Z_{HC} are mineral weight fraction, weight percent of Z in the mineral, and Z content in the hydrochar, respectively, where Z is P, Mg, or Ca.

2.4.2 Liquid-state NMR of biocrude and aqueous-phase coproduct. The biocrude samples (70–100 mg) were dissolved in 700 μL deuterated chloroform (99.8% $CDCl_3$ +0.03% v/v TMS, Cambridge Isotope Laboratories), added with deuterated benzene (99.5% C_6D_6, Cambridge Isotope Laboratories) and triphenyl phosphate as internal standards for ^{13}C and ^{31}P NMR, respectively. Meanwhile, the HTL-AP samples (65–110 mg) were dissolved in 700 μL deuterated dimethyl sulfoxide (99.9% d-DMSO +0.03% v/v TMS, Cambridge Isotope Laboratories), with 1,3,5-trioxane-$^{13}C_3$ (99%, Sigma Aldrich) and phosphonoacetic acid (TraceCERT, Supelco) as internal standards for ^{13}C and ^{31}P NMR, respectively. The ^{13}C and ^{31}P spectra were collected across 256 and 160 transients, respectively, using 500 MHz Bruker Avance II NMR spectrometer employing 5 mm inverse quadruple resonance probe and inverse-gated proton decoupling. The operating parameters are 90° pulse angle, sweep width of 30 kHz for ^{13}C and 10 kHz for ^{31}P, and relaxation delay of 30 s. The collected spectra were processed using MNova 14.2.3 (Mestrelab Research) with a mixture analysis plugin SMA 3.0 and the Wolfgang Robien NMR spectral database (Wiley) to quantify the composition of organic compounds and phosphorus functional groups. To verify the quantification results, the C, H, O, N, and P content estimated from the NMR-based organics and inorganics composition were compared with direct measurement using the elemental analyzers.

3 Results and discussion

Our structure is intended to first provide details on the characterization parts of our study that will be followed by our evaluation of proposed mechanistic reaction pathways. This section specifically is divided into three subsections. Subsection 3.1 presents the results of XRD characterization of hydrochar, which include the degree of crystallinity, the WPF and Rietveld refinements, and the organic and mineral phase composition. Subsections 3.2 discusses the results of experimentally-measured elemental content and chemical functionalities distribution in the hydrochar to validate the XRD phase compositions. Subsection 3.3 provides mechanistic explanations for the variations of detected organics and minerals in the hydrochar.

3.1 Hydrochar characterization using XRD

3.1.1 Crystallinity and refinement assessment. The hydrochar was mainly composed of highly crystalline organic and mineral phases, as indicated by the degree of crystallinity – a ratio of the total crystalline peaks area to the total XRD pattern area – that ranged between 79–93% (see Tables 1 and S4†). The high crystallinity allows the application of the WPF and Rietveld refinement methods without having to use an internal or external standard in quantifying the composition of organic and mineral phases of hydrochar based on the intensity of crystalline peaks in the XRD pattern.

The WPF and Rietveld refinement outcomes were assessed graphically and statistically by directly observing the conformity of the estimated and measured intensities and by calculating the fitting and refinement parameters, respectively. Fig. S2 and S3† shows the linear trend for the "$I_{obs} - I_{cal}$" line, which indicated the small discrepancies between the estimated and measured intensities.

Tables 1 and S4† show the most important statistical parameters to indicate the quality measure of Rietveld fitting, *i.e.*, R_{Bragg} and R_{WP} (see Tables S5 and S6† for the other refinement parameters). The R_{Bragg} for each detected phase in the hydrochars ranged between 5.67–10.83%, which indicated that the refinement was capable of reproducing the single-crystal crystallographic information. The R_{WP} for the full diffraction profile of all the hydrochars ranged between 10.14–14.95%, very close to the $R_{WP,expected}$, *i.e.*, 9.04–11.76%. These R_{WP} and $R_{WP,expected}$ results indicated that the full diffraction pattern processing using the WPF and Rietveld methods provided the calculated intensities that satisfactorily fitted with the measured intensities. Moreover, the satisfactory quality of fitting results confirmed that the refined phase-specific scale factors calculated from the whole pattern fitting (WPF) and Rietveld methods can be used to estimate the weight fraction of the detected phases in the hydrochars by including the corresponding crystallographic properties.

3.1.2 Organic phase composition. The weight fractions for the organic phase in the hydrochar ranged from 59.4 to 73.0%. Tables 1 and S4† reveal that the organic phases in hydrochars consisted of monocyclic, heterocyclic, and polycyclic aromatics with various aliphatic and aromatic substituents.

The acid-catalyzed HTL of lignin-rich digestate at lower temperature produced hydrochar with organic phases majorly comprised aromatic amines (*e.g.*, polyaniline and *N*,*N*-dimethyl-4-nitroaniline), hydroxynitrile (*e.g.*, 2-(4-hydroxyphenyl)-acetonitrile), benzoic acids (*e.g.*, indole-2-carboxylic acid·3,5-dinitrobenzoic acid), and alkoxy- and indoline-substituted nitrochromenes. At higher temperature, the organic phase comprised mostly polycyclic aromatic hydrocarbons (*e.g.*, 1-(anthracen-9-yl)-*N*-(phenylmethyl)methanaminium chloride), indoles (*e.g.*, 1*H*-indoline-2,3-dione), and quinones (*e.g.*, 2-aminoanthraquinone and 2,5-dihydroxy-1,4-benzoquinone).

Table 1 The WPF and Rietveld refinement results for diffractograms of hydrochar produced from HTL of lignin-rich digestates at pH 3.5 and 320–360 °C. Results for the other process conditions are given in Tables S4 and S6 in the ESI (PDF: Powder Diffraction File)

Operating conditions	PDF ID	Detected organic and mineral phases	Composition (wt%)	R_{Bragg} (%)	R_{WP} (%)	Crystallinity (%)
Cel/Lig 0.2 pH 3.5 320 °C	00-053-1717	Polyaniline	15.4 ± 1.1	6.34	10.14	75.93
	00-059-1090	1,2-Bis(2,6-dichlorobenzylidene)hydrazine	3.6 ± 0.6	7.28		
	00-055-1744	Ethyl-1′,3′,3′-trimethyl-8-nitrospiro[chromene-2,2′-indoline]-5′-carboxylate	7.1 ± 0.3	8.55		
	00-055-1827	Indole-2-carboxylic acid 3,5-dinitrobenzoic acid	8.5 ± 1.8	5.72		
	00-054-2291	3,5-Diamino-1*H*-1,2,4-triazole	2.7 ± 0.6	6.06		
	00-051-2369	3-Amino-4-(3-methoxyphenyl)-3,4,7,8-tetrahydro-2*H*-benzo[*e*][1,2]oxazin-6(5*H*)-one	4.5 ± 0.4	9.11		
	00-054-1622	2-(4-Hydroxyphenyl)acetonitrile	8.9 ± 0.9	8.35		
	00-015-0973	*N*,*N*-Dimethyl-4-nitroaniline	19.8 ± 0.4	8.06		
	00-009-0080	Monetite	17.2 ± 1.4	5.69		
	00-020-0669	Nesquehonite	12.2 ± 0.3	6.99		
Cel/Lig 0.2 pH 3.5 360 °C	00-048-2341	2-Aminoanthraquinone	7.2 ± 0.6	10.02	11.64	80.16
	00-062-1376	1-(Anthracen-9-yl)-*N*-(phenylmethyl)methanaminium chloride	10 ± 0.2	9.57		
	00-046-1758	2,5-Dihydroxy-*p*-benzoquinone	21.4 ± 0.7	8.75		
	00-055-1744	Ethyl-1′,3′,3′-trimethyl-8-nitrospiro[chromene-2,2′-indoline]-5′-carboxylate	4.9 ± 0.5	8.04		
	00-037-1955	1*H*-Indoline-2,3-dione	12.9 ± 1.0	7.11		
	00-043-1767	(*E*)-1,2-Dichloro-1,2-bis(5-phenyloxazol-2-yl)ethene	3 ± 0.8	5.67		
	00-009-0080	Monetite	9.7 ± 0.3	6.16		
	01-086-0175	Magnesite	11 ± 0.4	6.36		
	00-055-0898	β-Tricalcium phosphate	19.9 ± 0.8	7.25		

Meanwhile, under alkaline catalysis and at lower temperature, the hydrochar's organic phase was constituted of hydroxyaniline-substituted chromanediones, carbonitrile-substituted benzofurans, and dinitrophenoxy- and alkoxybenzylamine-substituted phenylpyrazolones. Moreover, at higher temperatures, polycyclic quinones (*e.g.*, 1,2-dihydroxyanthraquinone), amides (*e.g.*, 2-hydroxy-3-methyl-*N*-phenethylbutanamide), azoles (*e.g.*, 5-methyl-1*H*-tetrazole, 5-amino-3*H*-1,2,4-triazol-3-one, and ethene-1,1-diaminium-3-nitro-1*H*-1,2,4-triazol-5-olate), and phenoxyacids (*e.g.*, 3-(2,4,5-trichlorophenoxy)-propanoic acid) were the primary organic phases in the hydrochar. These composition profiles resulted in a decreasing and increasing trend of carbon and nitrogen content of hydrochar, respectively, with reaction temperature regardless of the catalysts (see Fig. 1). Meanwhile, the oxygen content of hydrochar showed an increasing and decreasing trend with temperature under acidic and alkaline catalysis, respectively.

Speciation of the organic elements in the hydrochar changed significantly when the feedstock contains more cellulose than lignin. On the one hand, acid catalysis at lower temperature promoted the precipitation of organics as amino-benzoxazines, hydroxypyranochromenones, alkyl-substituted cyclic ketones, indole- and pyrrole-carboxylic acid, and cycloalkane-carboxylic acid in the hydrochar. On the other hand, acid catalysis at higher temperature fixed less carbon and more oxygen and nitrogen into the hydrochar than that at lower temperature by forming derivatives of quinones, pyrroles, indazoles, and chromenes. Alkaline catalysis at both lower and higher temperatures precipitated the organics mostly as *N*-heterocyclics with *ortho*- and *para*-terphenyl configuration containing alkyl, benzoyl, and nitro substituents; therefore, more carbon and nitrogen and less oxygen were fixed in the hydrochar

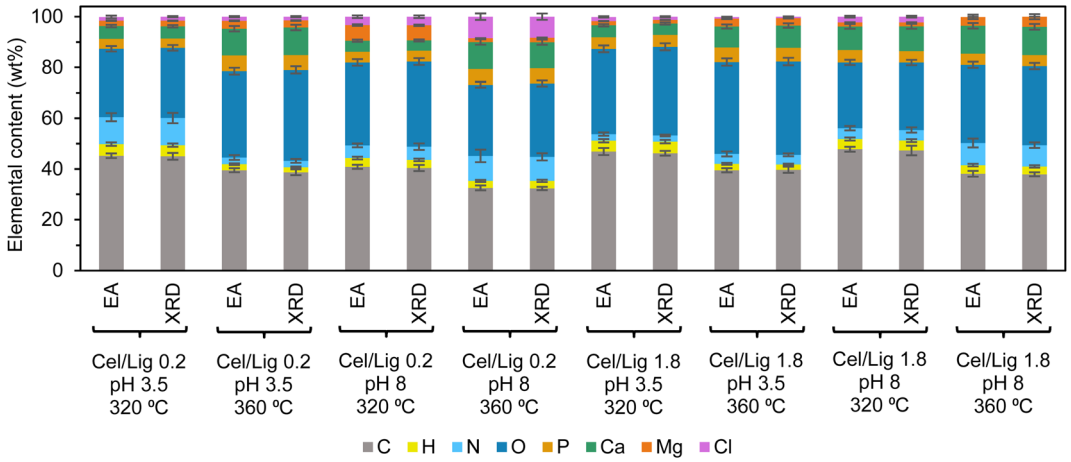

Fig. 1 Elemental content of hydrochar measured using the elemental analyzers (EA) and estimated using the XRD phase compositions.

compared to the acid catalysis (see Fig. 1). Lower temperature generated more azoles, methoxyanilines, and azaarenes in the hydrochar, *e.g.*, 3-methyl-5-phenoxy-1*H*-pyrazole-4-carboxamide, 4-(4-methoxy-2-methyl-phenethyl)-aniline, (5-chloro-2-nitrophenyl)(λ1-oxidaneyl)methanone·(4-methoxyphenyl)(pyridin-4-yl)methanone, and 1-methyl-4,5-diphenyl-3,4-dihydropyridin-2(1*H*)-one. Meanwhile, higher temperature produced more diazines, pyridine monoesters, azoles, and dioxoanthracenes in the hydrochar, *e.g.*, 2,3-di(pyridin-2-yl)pyrazine 1-oxide, methyl nicotinate, 3,3-diethyl-5-methyl-piperidine-2,4-dione, 5-methyl-1*H*-tetrazole, 5-amino-3*H*-1,2,4-triazol-3-one, and 1,2-dihydroxyanthraquinone.

3.1.3 Mineral phase composition. As seen in Tables 1 and S4,† the weight fractions for the mineral phases in the hydrochar ranged from 27.0 to 40.6%. The acid-catalyzed HTL of digestate produced hydrochars that always contained monetite ($CaHPO_4$, 7.5–17.2 wt%), β-tricalcium phosphate ($Ca_3(PO_4)_2$, 12.9–19.9 wt%), and magnesium-carbonates as primary mineral phases. The lower and higher temperature resulted in the speciation of magnesium-carbonate as nesquehonite ($MgCO_3 \cdot 2H_2O$, 9.4–12.2 wt%) and magnesite ($MgCO_3$, 6.9–11 wt%), respectively. In addition, acid catalysis at lower and higher reaction temperatures favored the formation of troemelite ($Ca_4P_6O_{19}$, 9.3–10.9 wt%) and calcium-phosphinate acetylene dicarboxylate decahydrate ($C_4H_8Ca_2O_{12}P_4 \cdot 10H_2O$, 5.4–6.0 wt%), respectively, when combined with higher cellulose-to-lignin ratio in the feedstock.

The mineral phases in the hydrochar produced from the alkali-catalyzed HTL were more complex and generally consisted of calcium-carbonates, apatites, and less-hydrated magnesium-carbonates, as shown in Tables 1 and S4.† The calcium-carbonates included calcite (trigonal $CaCO_3$, 9.3–9.9 wt%) at lower temperatures and aragonite (orthorhombic $CaCO_3$, 3.5–4.3 wt%) and vaterite (hexagonal $CaCO_3$, 3.2–3.8 wt%) at higher temperatures. The detected apatites were hydroxyapatite ($Ca_{10}(PO_4)_6(OH)_2$, 14.3–15.1 wt%) at lower temperature and A-type carbonated apatite ($Ca_{10}(PO_4)_6(CO_3)$, 16.0–24.3 wt%) and hydroxyapatite methyl phosphonic dichloride ($C_4H_{12}Cl_8O_4P_4 \cdot Ca_5(PO_4)_3(OH)$, 14.3–16.9 wt%) at higher temperature. In addition to apatites, Ca and P precipitated as calcium ethylenediammonium cyclotetraphosphate dihydrate ($C_2H_{10}CaN_2O_{12}P_4 \cdot 2H_2O$, 4.9–6.1 wt%) in the hydrochar when the feedstock was rich in lignin and had alkaline pH. The detected magnesium-carbonates were hydromagnesite ($Mg_5(CO_3)_4(OH)_2 \cdot 4H_2O$, 5.2–7.5 wt%) at lower temperature and pokrovskite ($Mg_2CO_3(OH)_2$, 4.1–5.4 wt%) and magnesite ($MgCO_3$, 6.9–11.0 wt%) at higher temperature. Besides, Mg also bound P as hydroxylwagnerite ($Mg_2(PO_4)OH$, 13.4–14.8 wt%) and whitlockite ($Ca_{18}Mg_2H_2(PO_4)_{14}$, 10.0–10.4 wt%) when the feedstock has lower and higher cellulose-to-lignin ratios, respectively.

3.2 Hydrochar characterization using elemental analysis and solid-state NMR methods

3.2.1 Elemental content. Fig. 1 shows that the estimated elemental content of hydrochar based on the organic and mineral phase composition from XRD analysis had similar values to the directly measured elemental content of using the high temperature combustion-reduction and EDX spectrometry techniques (see subsection 2.2). The relative error percentage between the XRD-estimated and directly-measured elemental content ranged between 0.2–0.8%, 0.1–0.5%, 0.1–0.4%, 0.3–1.9%, 0.1–0.4%, 0.2–0.5%, 0.1–0.5%, and 0–0.4% for C, H, N, O, P, Ca, Mg, and Cl, respectively. These results validate the use of XRD to determine phase compositions in terms of elemental speciation.

3.2.2 Carbon functional groups. The organic phase compositions of the hydrochars studied was validated based on the quantitative distribution of carbon functionalities determined from the relative area percentages of spectral peaks located on particular chemical shift regions on the ^{13}C SS-NMR spectra. The accuracy of the integration method used to calculate the spectral peak area was confirmed by the relatively close values between the NMR-predicted and directly-measured carbon content of hydrochar, (see Table S8†).

In general, the aliphatic and aromatic carbons located at 0–50 and 110–145 ppm, respectively, provided the largest

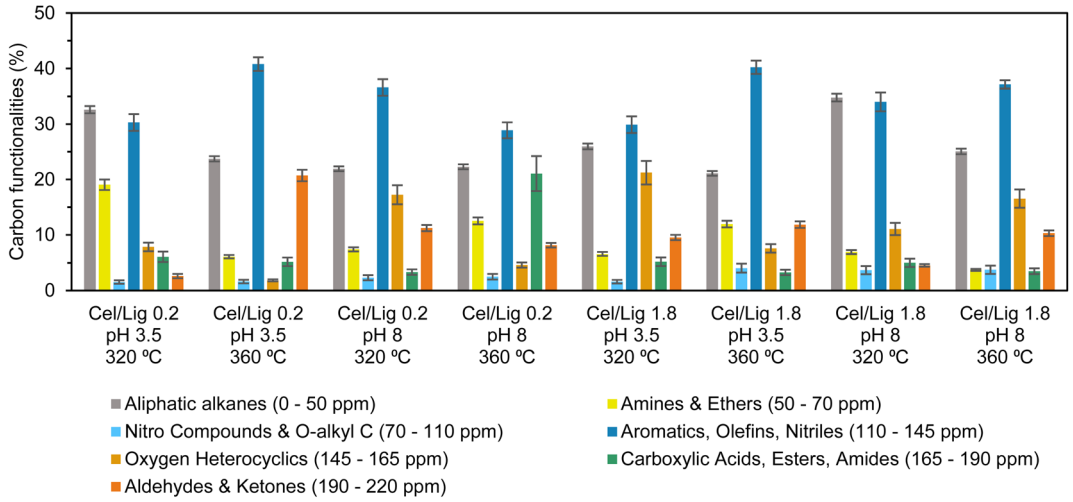

Fig. 2 Carbon functionalities distribution in the hydrochar based on quantitative DP-MAS ^{13}C SS-NMR. Fig. S4 in the ESI† shows the corresponding ^{13}C SS-NMR spectra.

contributions to the total carbon of hydrochar with an estimated proportion of 21.1–34.8% and 28.9–40.8%, respectively, as shown in Fig. 2. This result resonated with the primary chemical structure of the organic phase detected by the XRD, *i.e.*, monocyclic, polycyclic, and heterocyclic aromatics.

Fig. 2 also reveals a substantial contribution of carbon from amine and ether groups to the total carbon of hydrochar produced from the acid-catalyzed HTL of lignin-rich digestate at lower temperature, 19.05%, the highest among all the investigated conditions in this study. This result was associated with the high content of polyaniline and *p*-nitro-*N*,*N*-dimethylaniline and the appreciable presence of alkoxy substituents (see Table 1). Moreover, the ^{13}C SS-NMR spectra (see Fig. S4a†) showed several peaks with a significant intensity at 115.8, 145–165, and 165–180 ppm that were affiliated with the resonances of nitriles, *O*-heterocyclics, and carboxylic acids, respectively, confirming the presence of hydroxynitrile, benzoic acids, and alkoxy- and indoline-substituted nitrochromenes in the hydrochar produced from the same condition. Under acid catalysis conditions pH 3.5, and at higher temperature >320 °C, a significant amount of carbonyl carbon of ketones, 20.7% of total carbon, was observed at 190–220 ppm in addition to the carbon of amine substituents at 50.5 and 51.9 ppm (see Fig. S4b†), affirming the detection of aromatic ketones and amines by XRD, *e.g.*, 1-(anthracen-9-yl)-*N*-(phenylmethyl)methanaminium chloride, 2,5-dihydroxy-1,4-benzoquinone, 2-aminoanthraquinone, and 1*H*-indoline-2,3-dione.

The ^{13}C SS-NMR spectra of hydrochar from the alkaline-catalyzed HTL of lignin-rich digestate at lower temperature showed several singlets with strong signals at 145–165 and 190–220 ppm, as shown in Fig. S4c in the ESI.† These results were associated with a prominent proportion of carbon from *O*-heterocyclic (25.63%) and ketone (8.35%) groups, respectively, in addition to the dominant aliphatic (21.9%) and aromatic (36.6%) carbons. Similarly, at higher temperature, multiple sharp and intense singlets were observed at 50–70, 180.7, and 213.3 ppm (see Fig. S4d†) together with strong multiplets at 145–165 ppm, providing the relative proportions of 12.5%, 21.1% and 8.1% for carbons from –NCH (amine) or –OCH_3 (ethers), C–O (*O*-heterocyclics), and –COO (carboxylic acids) or N–C=O (amides) groups, respectively. These results supported the XRD analysis that discovered benzofurans, chromenediones, aromatic amides, and phenylpyrazolones in the hydrochar produced at lower temperature and hydroxyquinones, triazoles and tetrazoles, and aromatic esters and amides at higher temperature.

The ^{13}C SS-NMR spectra of hydrochar from the acid-catalyzed HTL of cellulose-rich digestate at lower temperature (see Fig. S4e†) showed strong signals for (1) the aromatic C–O of benzopyran and pyranochromenediones in the region of 145–165 ppm, (2) the –OCH_3, indole ring, and C=O of methoxyindole-substituted ketones at 56–65, 129.5, and 205.6 ppm, respectively, and (3) the five-membered ring and –COOH of cyclopentane- and pyrrole-carboxylic acids at 130.7–135.4 and 174.8 ppm, respectively. For the hydrochar produced under acid catalysis and at higher temperature, (1) the signals from the five-membered rings, C=O, and C–O of pyrroledione and indazolol were observed in 110–142, 200–220, 50–60 ppm regions, respectively, (2) the –NCH substituent and C=O of aminoanthraquinone at 52.4 and 194 ppm, respectively, and (3) the –NCH substituent and aromatic C–O of hydroxyaniline-substituted chromenediones at 56.9 and 150.2 ppm, respectively (see Fig. S4f†). Meanwhile, hydrochars derived from the alkaline-catalyzed HTL of cellulose-rich digestate produced ^{13}C SS-NMR spectra (see Fig. S4g and h†) with (1) significant signals for *N*-heterocyclic and anisyl rings in the 110–145 ppm region with high-intensity peaks at 111.9, 114.2, 120.45, 132.13, 137.2, and 139.1 ppm, (2) –COOR signals for esters of benzoate and nicotinate at 182.7 and 184.7 ppm, respectively, and –$CONH_2$ signal for carboxamide at 168 ppm, (3) C=O signals for pyridones, chromenediones, piperidinediones, and quinones in the region of 190–220 ppm, and (4) –OCH_3 and –NO_2 signals for

the ether and nitro substituents at 50–65 and 71.9 ppm, respectively. These chemical shift assignments, combined with the corresponding carbon functionalities distribution (see Fig. 2), are consistent with measured compositions of detected organic phases in the hydrochar resulting from the HTL of cellulose-rich digestate.

3.2.3 Mineral functional groups. The mineral phase composition provided by XRD were confirmed by the ^{31}P, ^{25}Mg, and ^{43}Ca SS-NMR analysis with the same quantification technique as the ^{13}C SS-NMR to determine the functionalities distribution, *i.e.*, spectral peak integration. The relative proportions of P, Mg, and Ca functional groups shown in Fig. S15† were validated by (1) the highly close values between the P, Ca, and Mg content of hydrochar that was estimated based on the total NMR spectral peaks area with those were directly measured using the EDX spectrometer (see Table S8†) and (2) the close values between the NMR and XRD estimation for percent contribution of P, Ca, and Mg from each mineral toward the total content of corresponding elements in the hydrochar (see Table S7†).

Fig. S8 in the ESI† showed that the ^{31}P spectra of hydrochars contained peaks at three different regions representing polyphosphates (−50 to −10 ppm), phosphates and phosphate esters (−5 to 10 ppm), and phosphonates (10–30 ppm).[55] The hydrochars generated from the acid-catalyzed HTL of digestate showed intense signals at (1) −4, 0.2, and 4.3 ppm, (2) −1.8 and 0 ppm, (3) 0.4 and 4.83 ppm, and (4) −36 ppm on the ^{31}P spectra because they contained calcium-phosphinate acetylene dicarboxylate decahydrate, monetite, β-tricalcium phosphate, and troemelite, respectively. These intense signals were reflected into prominent relative proportions of phosphates and phosphate esters in P functionalities that ranged between 40 and 100% (see Fig. S15†), confirming the domination of P speciation as phosphate and phosphate ester minerals in the hydrochar. Meanwhile, the hydrochars produced from the alkaline-catalyzed HTL of digestates showed significant singlets at −2.4 and 0, −35, 2.43, and 2.89 ppm on the ^{31}P spectra due to the presence of hydroxylwagnerite, calcium-ethylenediammonium cyclotetraphosphate dihydrate, whitlockite, and apatites, respectively. A singlet at 20 ppm was also observed with the 2.89 ppm peak when hydroxyapatite methyl phosphonic dichloride existed. These observed singlets provided relative proportions of phosphates and phosphate esters, polyphosphates, and phosphonates between 48–100%, 36–60%, and 50–54%, respectively (see Fig. S15†). These results indicated that alkaline conditions distributed chemical speciation of P in the hydrochar into not only phosphates and phosphate esters but also polyphosphates and phosphonates, in contrast to results obtained under acidic conditions that provided P mostly as phosphates and phosphate esters.

Fig. S8† also shows ^{25}Mg and ^{43}Ca spectra with different signal locations in the region of −20 to 30 ppm and −30 to 25 ppm, respectively, due to different chelated counter-anions or ligands and polymorphs. We classified the ^{25}Mg spectra into Mg–O groups representing Mg-phosphates (−30 to 0 ppm), Mg-carbonates (0–20 ppm), and Mg-hydroxides (20–40 ppm),[56] and ^{43}Ca spectra into Ca–O groups representing aragonite (−30 to −25 ppm), complexes of polyphosphates (−25 to −20 ppm), phosphates and phosphinates (−20 to 10 ppm), calcite and vaterite (10–20 ppm), and phosphonates (20–40 ppm).[57]

When the hydrochar contained nesquehonite and magnesite, the ^{25}Mg spectra showed two singlets at 6.65 and 7.1 ppm, respectively. These singlets were attributed to Mg–O group constructing the coordination between Mg^{2+} and CO_3^{2-}. The presence of hydromagnesite or pokrovskite resulted in two singlets in the region of 10–12 and 24–26 ppm on the ^{25}Mg spectra, which were associated with Mg–O bond of Mg^{2+} with carbonate and hydroxide ions, respectively. Meanwhile, the hydrochar containing hydroxylwagnerite or whitlockite produced ^{25}Mg spectra with similar singlets location at −17 and −4 ppm, indicating the Mg–O bond of Mg^{2+} and orthophosphates.

Calcite, aragonite, and vaterite, three different polymorphs of $CaCO_3$, produced three singlets at three different shifts on the ^{43}Ca spectra, *i.e.*, 19.1, −26.8, and 15 ppm, respectively (see Fig. S8†). The apatite minerals, whitlockite, and calcium-phosphinate decahydrate generated ^{43}Ca spectra with singlets concentrated in the 0–10 ppm region, whereas the phosphonate-substituted hydroxyapatite produced a singlet at 25 ppm. These chemical shifts variations were due to different Ca–O bonds formed by Ca^{2+} with orthophosphates, phosphinates, and phosphonates. Meanwhile, troemelite and calcium-ethylenediammonium cyclotetraphosphate dihydrate produced two singlets at −25 and −20 ppm on the ^{43}Ca spectra of the hydrochar, respectively, due to Ca–O complexes between Ca^{2+} and polyphosphates.

Fig. S15 in the ESI† summarizes the relative proportions of ^{24}Mg and ^{43}Ca. Acidic conditions generally led to speciation of Mg and Ca as Mg-carbonate and Ca-phosphate minerals. In contrast, alkaline conditions produced more diverse speciations of Mg and Ca including Mg-phosphates, Mg-hydroxides, and Ca-phosphates.

Results in subsections 3.2.2 and 3.2.3 demonstrated that the functionalities distribution of C, P, Ca, and Mg consistently agreed with the chemical structure and percent weight profiles of the organic and mineral phases detected by XRD. These results confirmed the precision of the WPF and Rietveld methods in processing the XRD pattern to determine the composition of organics and inorganics in the hydrochar, providing detailed information on chemical structure of elemental speciation that cannot be obtained using the previously existing methods of hydrochar characterization.

3.3 Mechanistic interpretation

The proposed elemental speciation pathways were created by combining theoretical chemistry and heuristic graph-based approach using a cheminformatic software MØD.[58] First, we defined a set of reaction rules including (1) chemical species of the reactants (*i.e.*, cellulose, lignin, ammonia, glutamic acid, and minerals), intermediates in the biocrude and HTL-AP (see Tables S10–S25†), and phases in the hydrochar (see Table S4†) and (2) a list of probable reactions with their propensities based on previously reported mechanisms in the HTL literature. The

combinatorial enumeration of molecular graphs produced a set of probable molecular structures that can be generated from the reactants and intermediates. Second, we connected molecules from the resulting graphs with each other and with detected compounds in the hydrochar to acquire hypothetical elementary reaction paths, leading to a full reaction network. Ultimately, we assessed the feasibility of each path based on the estimated Gibbs free energy by eQuilibrator[59] to obtain a final reaction network. The comprehensiveness of the final reaction networks was confirmed by the acquired yield of products and elements (see Fig. S9–S14†) and the relatively close values between the products elemental (*i.e.*, C, H, N, P, Ca, and Mg) content directly measured using the elemental analyzers and the one estimated from the NMR-based organics/inorganics composition and XRD-based phase content (see Tables S8 and S9†). Thus, the proposed mechanistic pathways offer a more complete and consistent picture of chemical events associated with hydrochar formation than our earlier study focusing on the formation mechanisms of organics/inorganics in the biocrude and HTL-AP.[2]

The final reaction pathways are summarized in Fig. 3, 4, and 5 where each reaction pathway is labelled with C#, L#, and M#, respectively, with # is the reaction number. This label is referred close to the corresponding sentence to allow easier navigation to the discussed reaction pathway in the figure.

3.3.1 Organic phase from lignin-rich digestates. Fig. 3 and 4 show that phenols and aromatic acids, the lignin depolymerization products, are precursors for the detected organics in the hydrochar produced from HTL of lignin-rich digestate. The phenolic or phenolic-derivative compounds that are instrumental in the formation of hydrochar under acid catalysis included (1) phenol, (2) hydroquinone, (3) *p*-hydroxybenzoic acid, (4) acetophenone, (5) 3-methoxyphenol, (6) 2,5-dihydroxy-3,6-dimethyl-benzaldehyde, and (7) 4-(hydroxymethyl)-phenol. Lower temperature promoted amination (L6) and hydroxyformylation (L14) of phenol into aniline[60] and 4-(hydroxymethyl)-phenol,[41] respectively. Subsequently, aniline

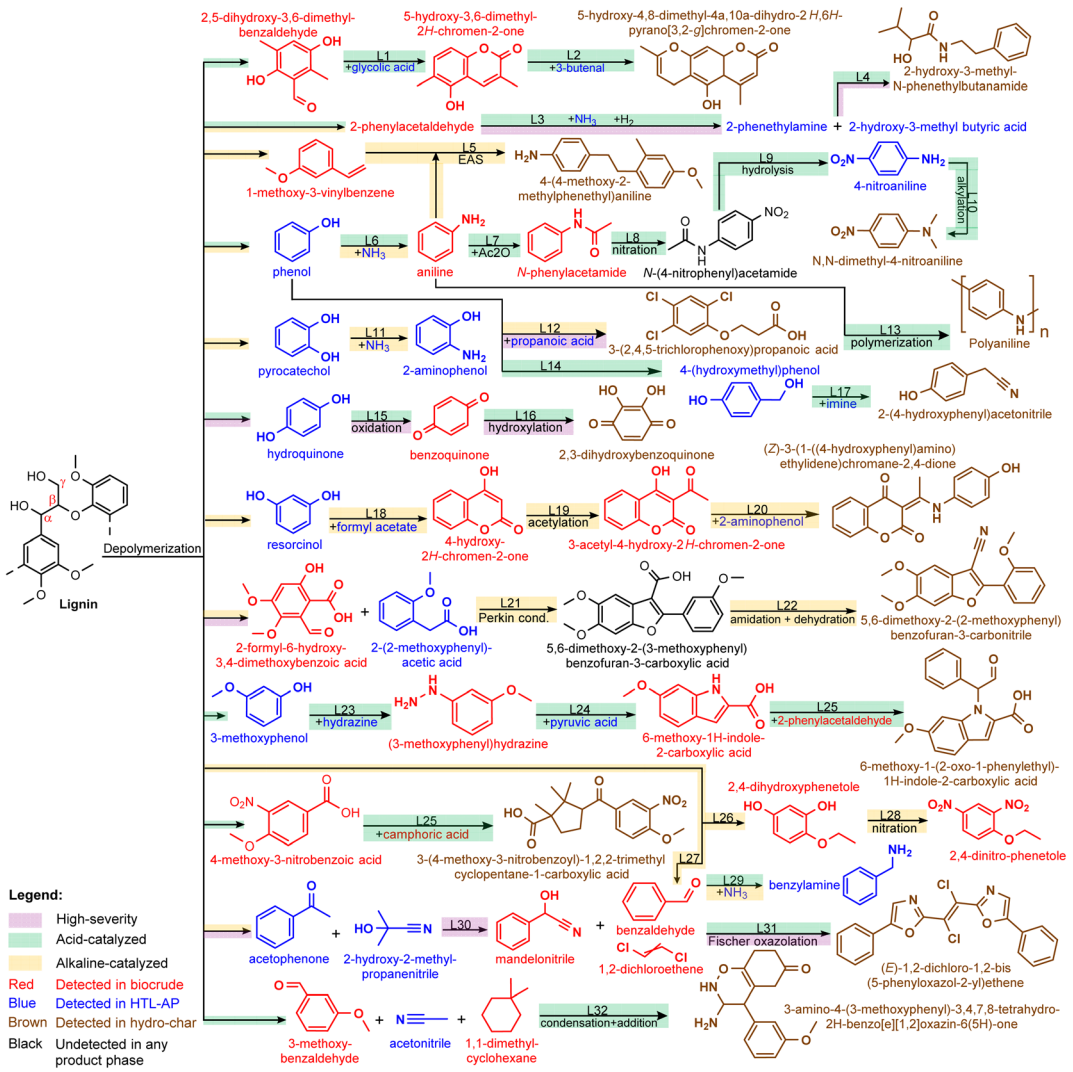

Fig. 3 Proposed mechanism for the precipitation of organics in the hydrochar involving the lignin depolymerization products as precursors. Each pathway is labelled L#, where # is the reaction number.

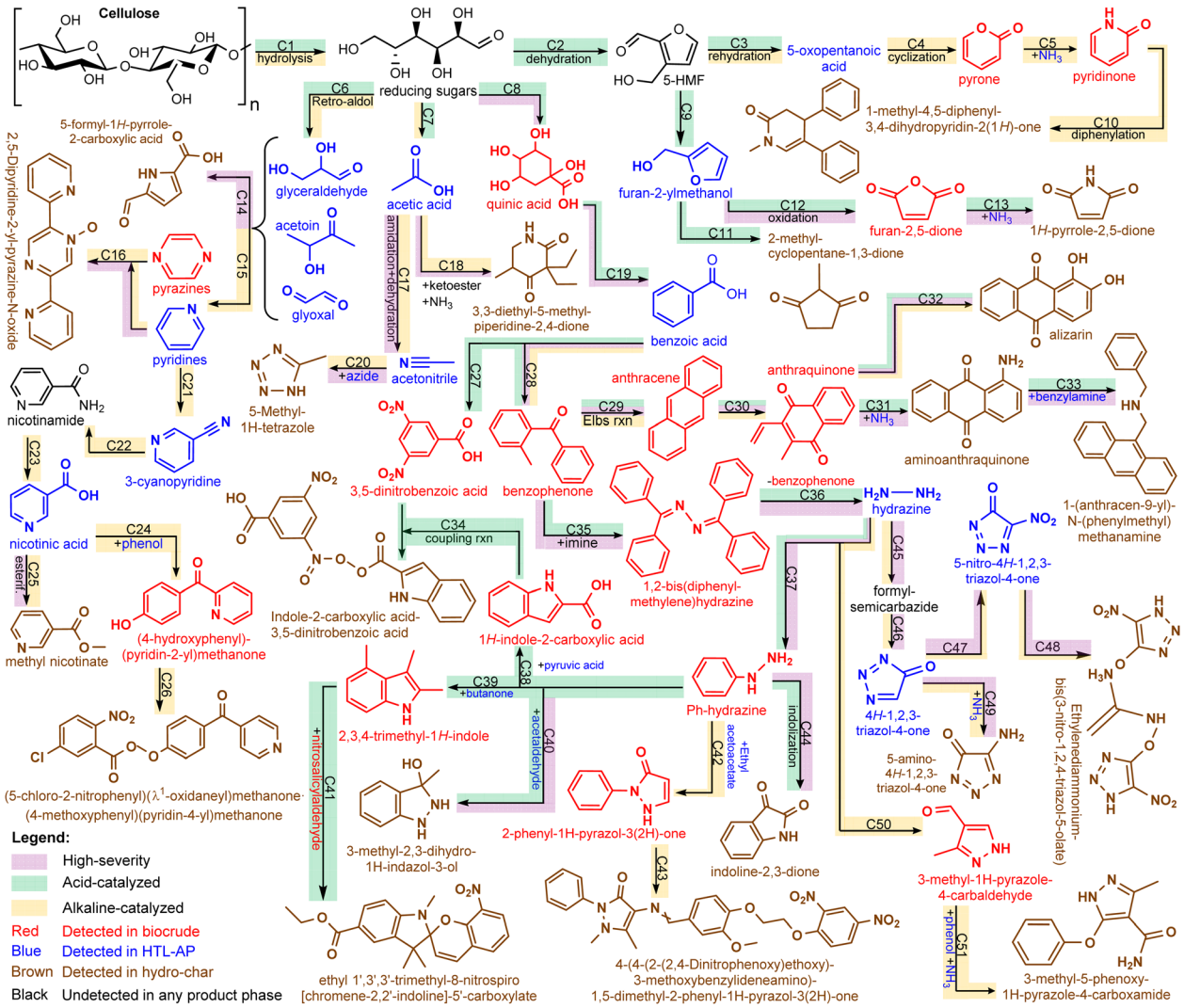

Fig. 4 Proposed mechanism for the precipitation of organics in the hydrochar involving the cellulose decomposition products as precursors, including benzoic acid that can be derived from lignin. Each pathway is labelled C#, where # is the reaction number.

oxidatively polymerized (L13) into solid polyaniline[61] and also experienced a sequence of reactions to precipitate as *N*,*N*-dimethyl-4-nitroaniline, *i.e.*, electrophilic aromatic substitution, nitration, hydrolysis, and alkylation reactions (L7–L10).[62] Meanwhile, 4-(hydroxymethyl)-phenol was oxidized by imine (L17), the product of ammonia condensation with ketones, into 2-(4-hydroxyphenyl)-acetonitrile in the hydrochar.[63]

Imines, such as benzophenone-imine derived from lignin-based *p*-hydroxybenzoic acid (C28), may also oxidatively coupled (C35) with each other to afford N–N-coupled benzophenone-azine, which was hydrolysable (C36) to produce hydrazine and regenerate the benzophenone.[64] While hydrazine was not detectable by ^{13}C NMR, its presence was confirmed by colorimetric measurement of HTL-AP following the ASTM D1385 method (see Table S3†).[65] The generated hydrazine may condense with phenol-derived C_6-cyclic ketones followed by tautomerization and dehydrogenation reactions to give phenylhydrazine (C37).[66] The reactivity of phenylhydrazine with α-dicarbonyl/α-hydroxycarbonyl and pyruvic acid *via* Fischer indolization mechanism were enhanced under acidic conditions to afford 2,3,4-trimethyl-1*H*-indole (C39) and 1*H*-indole-2-carboxylic acid (C38), respectively.[67] The former may further experience regioselective ethoxy-carbonylation with diethylazodicarboxylate,[68] ethylenation, and finally ring closure involving the ethylene group and the aldehyde and –COOH groups of 6-nitrosalicylaldehyde (C41) to precipitate as ethyl-1′,3′,3′-trimethyl-8-nitrospiro[chromene-2,2′-indoline]-5′-carboxylate.[69] The latter may couple with 3,5-dinitrobenzoic acid from nitration of benzoic acid and precipitated as indole-2-carboxylic acid·3,5-dinitrobenzoic acid (C34). The presence of nitrating agent was confirmed by colorimetric analysis of HTL-AP using the APHA 4500-NO_3 method (see Table S3†).[51]

Under acid catalysis at higher temperature, oxidation reaction possessed a more significant role in hydrochar formation. The oxidative depolymerization of lignin led to producing

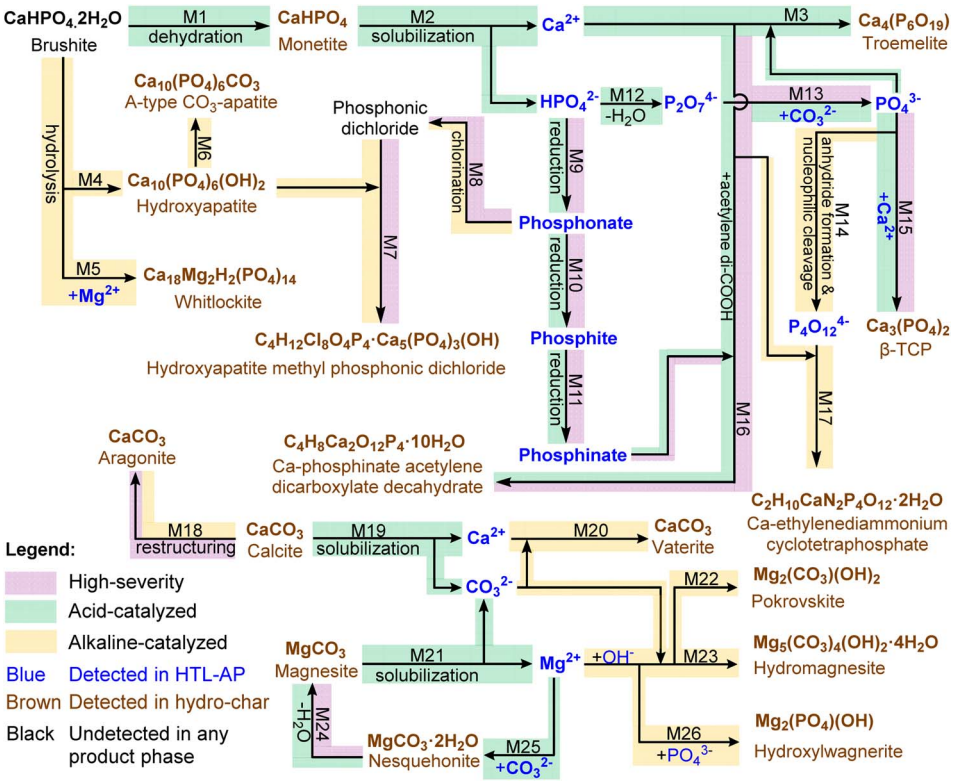

Fig. 5 Proposed mechanism for the precipitation of minerals in the hydrochar. Each pathway is labelled M#, where # is the reaction number.

hydroquinone, 4-hydroxybenzoic acid, and acetophenone.[41] Subsequent oxidation of hydroquinone (L15) afforded benzoquinone,[70] which precipitated as 2,3-dihydroxybenzoquinone after dihydroxylation (L16). Likewise, 4-hydroxybenzoic acid was converted into benzophenone *via* oxidation-benzoylation mechanism (C28).[71] Afterward, the resulting benzophenone was dehydrated (C29, the Elbs reaction)[72] into anthracene followed by oxidation (C30) and amination[60] (C31) to precipitate as aminoanthraquinone. By coupling (C33) with benzaldehyde-derived benzylamine (L29), the aminoanthraquinone was further converted into solid 1-(anthracen-9-yl)-*N*-(phenylmethyl) methanamine. Indoles generated *via* Fischer indolization[73] were also oxidized into solid indoline-2,3-dione (C44) in the hydrochar. Meanwhile, acetophenone underwent addition reaction with 2-hydroxy-2-methyl-propanenitrile (L30) to yield mandelonitrile, which was ultimately converted into solid (*E*)-1,2-dichloro-1,2-bis(5-phenyloxazol-2-yl)ethene *via* Fischer oxazole reaction (L31) with benzaldehyde and dichloroethene.[74]

Under alkaline catalysis, the key intermediates for hydrochar formation were the fragmentation products of lignin *via* cleavage of the β-O-4 ether bonds, *i.e.*, resorcinol, pyrocatechol, benzoic acid, 2-formyl-6-hydroxy-3,4-dimethoxybenzoic acid, 2-phenylacetaldehyde, *o*-vanillin, and 2,4-dinitrophenetole.[41] At lower reaction temperature, there were three main reaction pathways that converted several of those compounds into three major organics groups in the hydrochar, *i.e.*, aniline-chromanediones, dinitrophenoxy-substituted phenyl-pyrazolones, and carbonitrile-substituted benzofurans. The first pathway was the Pechmann condensation of resorcinol with formyl acetate (L18) producing 4-hydroxy-2*H*-chromen-2-one in the biocrude.[75] Acetylation of this compound (L19) into 3-acetyl-4-hydroxy-2*H*-chromen-2-one[76] allowed the formation of (*Z*)-3-(1-((4-hydroxyphenyl)amino)ethylidene)chromane-2,4-dione in the hydrochar because the acetyl group was susceptible to condensation (L20) with the amine group of 2-aminophenol, *i.e.*, the amination product of catechol.[77] The second pathway was regioselective nucleophilic addition involving a nitrogen atom of benzoic acid-derived phenylhydrazine with carbonyl carbon of ethylacetoacetate,[78] followed by intramolecular cyclization with the ester group of ethylacetoacetate and the other nitrogen atom of phenylhydrazine to produce phenylpyrazolone (C42). Phenylpyrazolone readily precipitated as 4-(4-(2-(2,4-dinitrophenoxy)-ethoxy)-3-methoxy-benzylidene-amino)-1,5-dimethyl-2-phenyl-1*H*-pyrazol-3(2*H*)-one in the hydrochar through sequential condensation reactions with *o*-vanillin and 2,4-dinitrophenetole (C43).[79] The third pathway was the Perkin aldol condensation between 2-formyl-6-hydroxy-3,4-dimethoxybenzoic acid and 2-(2-methoxyphenyl) acetic acid (L21) producing 5,6-dimethoxy-2-(3-methoxyphenyl) benzofuran-3-carboxylic acid intermediate in the biocrude.[80] The conversion of its carboxylic group into carbonitrile (L22) *via* amidation reaction with highly-nucleophilic ammonia followed by dehydration resulted in precipitation in the hydrochar.[81]

Alkaline catalysis at higher reaction temperature showed three primary reaction pathways that led to four dominant groups of organics in the hydrochar, *i.e.*, amides, phenoxyacids,

quinones, and azoles. Condensation reaction (L3–L4) involving 2-phenylacetaldehyde, ammonia, and cellulose-derived 2-hydroxy-3-methyl butyric acid was responsible for the formation of 2-hydroxy-3-methyl-*N*-phenethylbutanamide in the hydrochar.[82] Similarly, 3-(2,4,5-trichlorophenoxy)-propanoic acid precipitated through condensation of phenol with propanoic acid (L12). Meanwhile, the formation of 1,2-dihydroxyanthraquinone followed the same mechanisms as 1-aminoanthraquinone at high temperature acid-catalyzed HTL with the amination step was replaced by the oxidation of C–H bond on the ring into C–OH (C32). This partial similarity was due to endothermic nature of the oxidation-benzoylation of benzoic acid into benzophenone[71] and the following dehydration[72] and oxidation.[83]

The formation of azoles particularly triazolones and tetrazoles generally followed the 1,3-dipolar cycloaddition mechanism. On the one hand, nucleophilic cycloaddition of formyl semicarbazide (*i.e.*, the product of deamination reaction between hydrazine and amides) to formic acid (C45) produced aqueous-phase 4*H*-1,2,4-triazol-5-one, which was converted into solid 5-amino-3*H*-1,2,4-triazol-3-one and aqueous-phase 5-nitro-4*H*-1,2,3-triazol-4-one *via* amination (C49) and nitration (C47) steps, respectively.[84] The 5-nitro-4*H*-1,2,3-triazol-4-one may precipitate as ethene-1,1-diaminium 3-nitro-1*H*-1,2,4-triazol-5-olate by reacting with ethylenediamine (C48) obtained from the reaction between dichloroethane and ammonia. On the other hand, the 5-methyl-1*H*-tetrazole formation *via* 1,3-dipolar cycloaddition (C20) involved acetic acid-derived acetonitrile (C17) and sodium azide, which was obtained through the Wislicenus reaction involving nitrite ester and hydrazine.[85] The presence of nitrites in HTL-AP was confirmed by colorimetry following the APHA 4500-NO_2 method (see Table S3†).[51]

3.3.2 Organic phase from cellulose-rich digestates. According to the structural chemistry of cellulose and traditional understanding of cellulose depolymerization products, the composition of organics in the hydrochar from the HTL of cellulose-rich digestate was expected to be more affected by α-dicarbonyls, α-hydroxycarbonyls, furans, pyrones, and carboxylic acids despite consistent participation of lignin depolymerization products, *i.e.*, 2-phenylacetaldehyde, 4-methoxy-3-nitrobenzoic acid, 3-methoxyphenylhydrazine, 3-methoxybenzaldehyde, 1-methoxy-3-vinylbenzene, and 2,5-dihydroxy-3,6-dimethyl-benzaldehyde (see Fig. 4). The key cellulose-derived precursors for hydrochar formation in the acid-catalyzed HTL of cellulose-rich digestate were 2,5-hexanedione, furan-2-ylmethanol, pyruvic acid, glycolic acid, benzoic acid, 3-butenal, 2-propenal, and 1,3,5-benzenetriol whereas in the alkaline-catalyzed were 2-methylbutanal, acetaldehyde, glyoxal, 5-oxopentanoic acid, ethylacetoacetate, and acetic acid.

Acid-catalyzed HTL at lower reaction temperature accelerated Paal–Knorr reaction between 2,5-hexanedione and ammonia (C14) into solid 5-formyl-1*H*-pyrrole-2-carboxylic acid[86] and Piancatelli rearrangement of furan-2-ylmethanol (C11) into 2-methyl-cyclopentane-1,3-dione precipitate.[87] The Piancatelli rearrangement of furan-2-ylmethanol (C11) also produced 1,2,2-trimethyl-cyclopentane-1,3-dione in the biocrude, which was easily oxidized into 1,2,2-trimethyl-cyclopentane-1,3-dioic acid (camphoric acid). The Friedel craft condensation of camphoric acid with 4-methoxy-3-nitrobenzoic acid (L25) precipitated 3-(4-methoxy-3-nitrobenzoyl)-1,2,2-trimethyl-cyclopentane-1-carboxylic acid.[88]

The Fischer indolization involving pyruvic acid and 3-methoxyphenylhydrazine[73] (L24) and the Perkin reaction between glycolic acid and 2,5-dihydroxy-3,6-dimethyl-benzaldehyde[80] (L1) were also enhanced at lower HTL temperature. The Fischer indolization product, 6-methoxy-1*H*-indole-2-carboxylic acid may further condense into solid 6-methoxy-1-(2-oxo-1-phenylethyl)-1*H*-indole-2-carboxylic acid by reacting with 2-phenylacetaldehyde (L25). Meanwhile, the Perkin reaction product, 5-hydroxy-3,6-dimethyl-2*H*-chromen-2-one may further react with 3-butenal *via* Michael addition scheme followed by nucleophilic cyclization by the chromene's –OH group (L2) to afford solid 5-hydroxy-4,8-dimethyl-4*a*,10*a*-dihydro-2*H*,6*H*-pyrano[3,2-*g*]chromen-2-one.[89] In tandem with the Knoevenagel condensation of 3-methoxy-benzaldehyde with acetonitrile producing 4-(3-methoxyphenyl)-2*H*-benzo[*e*][1,2]oxazin-3-amine, the Michael addition involving 2-propenal may also precipitate 3-amino-4-(3-methoxyphenyl)-3,4,7,8-tetrahydro-2*H*-benzo[*e*][1,2]oxazin-6(5*H*)-one in the hydrochar (L32).[90]

Under acid catalysis at higher temperature, the oxidation reaction (C12) was more dominant than Piancatelli rearrangement to convert furan-2-ylmethanol, as evidenced by a higher concentration of furan-2,5-dione in the biocrude. The resulting furan-2,5-dione may react with ammonia, opening the cyclic chain and then forming maleamic acid that was readily cyclized into 1*H*-pyrrole-2,5-dione (C13) in the hydrochar.[91] Moreover, the same benzoic acid-derived products as HTL of lignin-rich digestate were observed in the biocrude, *i.e.*, aminoanthraquinone and 2,3-dihydroxybenzoquinone. While the reaction pathways were similar, the origin of benzoic acid was different in the HTL of cellulose-rich digestate. The benzoic acid was obtained through dehydroxylation of quinic acid, a biocrude component obtained *via* the condensation–dehydration reactions of erythrose with pyruvic acid (C8).[92] The presence of benzoic acid allowed the formation of phenylhydrazine, which can react with glucose-derived acetaldehyde *via* cycloaddition scheme (C40) producing 3-methyl-2,3-dihydro-1*H*-indazol-3-ol in the hydrochar.[93]

Alkaline conditions catalyzed the hydrochar formation by increasing the nucleophilicity of amine, ammonia, hydrazine, enolate-containing compounds, and azide. At lower reaction temperature, the presence of highly-nucleophilic amine or ammonia may attack the carbonyl carbon of α-dicarbonyls/α-hydroxycarbonyls to produce six-membered *N*-heterocyclics *via* Maillard reaction pathway (C15), *e.g.*, pyridine.[94] Pyridines may further experience oxidative ammonolysis (C21) and hydrolysis (C22) into nicotinamide intermediate,[95] which was deaminated into nicotinic acid (C23). Radical addition of nicotinic acid to the phenol ring (C24) resulted in the formation of (4-hydroxyphenyl)(pyridin-2-yl)methanone, which precipitated as (5-chloro-2-nitrophenyl)(λ1-oxidaneyl)methanone·(4-methoxyphenyl) (pyridin-4-yl)methanone. The highly nucleophilic ammonia may also participate in the exchange reaction (C5)

with the cyclization (C4) product of 5-oxopentanoic acid (*i.e.*, 2-pyrone) producing 2-pyridone and in the amination (L6) of phenol producing aniline.[60] Subsequently, the diphenylation of 2-pyridone with benzene (C10) yielded 1-methyl-4,5-diphenyl-3,4-dihydropyridin-2(1*H*)-one in the hydrochar,[96] while the electrophilic aromatic substitution of aniline with 1-methoxy-3-vinylbenzene (L5) precipitated 4-(4-methoxy-2-methyl-phenethyl)aniline.[97] Meanwhile, highly-nucleophilic hydrazine was involved through cyclocondensation with cellulose-derived methyl butanal (C50) producing 3-methyl-1*H*-pyrazole-4-carbaldehyde intermediate.[98] This intermediate was prone to nucleophilic addition by phenolate ion (C51) to precipitate as 3-methyl-5-phenoxy-1*H*-pyrazole-4-carboxamide.[82]

Similar trend was observed at higher reaction temperature at which the formation of *N*-heterocyclics (*i.e.*, pyridines and pyrazines) *via* Maillard reaction pathway (C15) was prominent. The same derivation route of pyridine into nicotinic acid (C21–C23) was also observed according to the detected intermediates in the biocrude and aqueous-phase products. The esterification of nicotinic acid into methyl nicotinate (C25) allowed the precipitation in the hydrochar. Moreover, pyridine and pyrazine may also couple *via* reductive coupling reaction followed by oxidation of a nitrogen atom of pyrazine (C16), producing solid 2,3-di(pyridin-2-yl)pyrazine 1-oxide.[99] The formation of diketone derivative of piperidine also occurred in the hydrochar, *i.e.*, 3,3-diethyl-5-methylpiperidinedione. While this compound contained the piperidine ring, its formation followed the Dieckmann cyclization mechanism[100] instead of Maillard reaction. The cyclization (C18) started with the enamine production involving β-ketoester, nucleophilic ammonia, and acetic acid. The tandem reduction–condensation reactions converted the enamine into β-amino ester, which readily cyclized to afford piperidinedione. In addition, azoles including 5-methyl-1*H*-tetrazole and 3-amino-1,2,4-triazol-5-one also existed in the hydrochar due to the increased nucleophilicity of azide that accelerated the 1,3-dipolar cycloaddition reaction (C17 and C46–C49) with carboxylic acids or nitriles.[85,101]

3.3.3 Mineral phase. Fig. 5 shows that acid catalysis dehydrated brushite (M1), the initial P speciation in the digestates, into monetite. In addition, acid catalysis may dissociate (M2, M19, and M21) the native minerals in the digestates into Ca^{2+}, Mg^{2+}, HPO_4^{2-}, and CO_3^{2-}. The ^{31}P NMR spectra (see Fig. S7†) shows that the HPO_4^{2-} may be dehydrated (M12) into pyrophosphate ($P_2O_7^{4-}$), and subsequently reacted with CO_3^{2-} (M13) producing orthophosphate (PO_4^{3-}). The PO_4^{3-} may precipitate with Ca^{2+} as troemelite (*via* condensation, M3) and β-TCP (*via* ionic coordination, M15) at lower and higher reaction temperatures, respectively. Noteworthy was that the formation of troemelite only occurred in the acid-catalyzed HTL of cellulose-rich digestates. The acid-catalyzed retro-aldol condensation of cellulose produced aliphatic carboxylic acids that are proton donors hastening the formation of troemelite.[102] The aliphatic acids may also serve as hydrogen donor after decomposition at higher temperature, promoting the endergonic reduction (M9–M11) of HPO_4^{2-} into phosphonate (RPO_3^{2-}), phosphite (HPO_3^{2-}), and finally phosphinate ($R_2PO_2^{-}$),[103] as shown by the ^{31}P spectra of HTL-AP (see Fig. S7f†). The acquired phosphinate may react with Ca^{2+} and acetylene dicarboxylic acid (M16) forming calcium-phosphinate acetylene dicarboxylate decahydrate precipitate. Meanwhile, the Mg^{2+} may easily chelate CO_3^{2-} and precipitate as nesquehonite (M25) because the cation coordination in the solid-state resembled the solution speciation. However, higher temperature activated the dehydration of nesquehonite into anhydrous magnesite (M24), the most stable magnesium-carbonate phase.

Alkaline catalysis hydrolyzed brushite into hydroxyapatite and whitlockite at lower temperature (M4–M5).[104] Moreover, the formed hydroxyapatite may be derived into A-type carbonated apatite and hydroxyapatite methyl phosphonic dichloride at higher temperature. The former was formed by the integration of CO_3^{2-} into the apatite lattice replacing the hydroxide (M6).[105] The latter was formed by the organic–inorganic bonding (M7) between the surface –OH groups of hydroxyapatite and methyl phosphonic dichloride.[106] The methyl phosphonic chloride may originate from chlorination of an endergonic reduction product of HPO_4^{2-}, *i.e.*, phosphonate (see Fig. S7d†).

Since the alkaline degradation pathway of cellulose generated acids through benzilic rearrangement of α-dicarbonyls,[2] the dissociations of digestate minerals were also observed. The dissolved orthophosphates may cyclize into cyclotetraphosphate ($P_4O_{12}^{4-}$), as evidenced by the ^{31}P spectra of HTL-AP (Fig. S7c†), by first forming phosphoric anhydride *via* oxygen bonding with three other orthophosphates followed by nucleophilic cleavage of the anhydride bond by alcohols (M14).[107] The ionic interaction among $P_4O_{12}^{4-}$, Ca^{2+}, and ethylenediammonium may result in the precipitation of calcium ethylenediammonium cyclotetraphosphate dihydrate. The alkaline-catalyzed HTL may also overcome the high energy barrier for the aggregation, dehydration, and extensive ionic rearrangement of Mg^{2+}, CO_3^{2-}, and OH^- to form less-hydrated magnesium-carbonates (M22–M23), *i.e.*, hydromagnesite, pokrovskite, and magnesite.[108] Similarly, the coordination chemistry of Mg^{2+}, PO_4^{3-}, and OH^- to form hydroxylwagnerite (M26) favored alkaline conditions.

The formation of orthorhombic and hexagonal polymorphs of $CaCO_3$ was also triggered by the high temperature-high pressure and hydrophile-rich systems under alkaline conditions. The high temperature-high pressure conditions induced endothermic reorientation (M18) of the Ca atom packing from trigonal (calcite) to orthorhombic (aragonite).[109] Meanwhile, high concentration of hydrophilic molecules (*e.g.*, phenols and acids) depleted free water molecules, significantly reducing solubility of the initially established hexagonal $CaCO_3$ polymorph (M20), *i.e.*, vaterite. With lower solubility, the transformation of vaterite into more thermodynamically-stable polymorph (calcite) through solubilization and reprecipitation was blocked.[110]

4 Conclusions and implications for hydrochar utilization

Understanding elemental speciation is critical for sustainable valorization of hydrochar derived from hydrothermal

liquefaction (HTL) of anaerobic digestates as a key part of processes that bring us closer to achieving a circular bioeconomy. We have taken detailed analyses of hydrochar using XRD, SS-NMR, and elemental analyzers and used the characterization data of all the HTL products to evaluate the mechanisms associated with the effects of HTL reaction temperatures (320–360 °C), feedstock pH (3.5–8), and feedstock cellulose-to-lignin ratios (Cel/Lig 0.2–1.8) on the chemical transformation and composition of organic and mineral phases in hydrochar. Mechanistic pathways developed using theoretical chemistry and heuristic graph-based approach incorporating appropriate thermodynamic constraints demonstrated that the organic precursors of hydrochar are organic species in biocrude and aqueous phases derived from depolymerization of cellulose and lignin, while the inorganic precursors majorly come from dissolved minerals in the aqueous phase. Lignin-derived precursors including phenols, benzaldehydes, and aromatic acids triggered the formation of hydrochar with a high oxygen content under acid catalysis at 320–360 °C because they readily undergo Perkin and Knoevenagel condensations, Michael addition, and Fischer oxazole reactions, leading to selective precipitation of *O*-heterocyclics, *i.e.*, benzofurans, benzopyran, oxazoles, and oxazines with ether substituents.

Furthermore, the employment of alkaline catalysis and higher temperature fixes more nitrogen into the hydrochar due to the addition of amine, nitrile, and nitro substituents onto the *O*-heterocyclic ring of benzofurans and benzopyran *via* Pechmann condensation, amidation–dehydration, and nitration reactions. Similarly, alkaline catalysis increases the reactivity of cellulose-derived precursors (*e.g.*, α-dicarbonyls and α-hydroxycarbonyls, furans, pyrones, and carboxylic acids) to selectively chelate nitrogenous species and precipitate as azaarenes with the aromatic ring composed of 1–4 nitrogen atoms (*e.g.*, pyridines, pyrroles, pyrazoles, triazoles, and tetrazoles) *via* 1,3-dipolar cycloaddition, Dieckmann cyclization, and Maillard reaction routes.

In contrast, acid catalysis at higher temperature suppresses *N*-fixing reactions involving the cellulose-derived precursors by allowing only the Fischer reaction forming indoles to occur, in addition to enhancing the Elbs dehydration of benzophenones to precipitate more polycyclic aromatics (*e.g.*, anthracenes and anthraquinones) that lead to improving the carbon recovery in hydrochar. Moreover, acid catalysis is beneficial for reducing the complexity of inorganic composition in hydrochar as its role during HTL is concentrated to dehydration of phosphate minerals into monetite, dissolving the minerals into the aqueous phase, and reprecipitation of hydrated magnesium-carbonates and tricalcium phosphate. On the other hand, alkaline catalysis has diverse roles including hydrolysis of brushite into apatite phosphate and whitlockite, hydroxylation producing pokrovskite, hydromagnesite, and hydroxylwagnerite, conversion of phosphates into cyclotetraphosphate, and rearrangement of hydroxyapatite into carbonated-apatite and calcite into aragonite and vaterite.

These elemental speciations demonstrated that traditional utilization of hydrochar as solid fuel, soil amendment/fertilizer, and water pollutant adsorbent may face environmental challenges due to potential NO_x emission after combustion, phytotoxicity, low nutrient bioavailability (*i.e.*, due to low solubility nature of the minerals), and hazardous chemicals leaching. These challenges may limit deployment due to regulations and higher costs. Alternatively, considering the chemical structure of the aromatics and minerals, more advanced valorization routes to produce organic semiconductor polymers, catalyst supports, flue gas (CO_2) adsorbents, pharmacologically-active compounds, biodegradable scaffolds, natural dyes, and coatings on metallic prosthesis may offer more profitable and sustainable outcomes in the short term. While future studies focusing on the development of efficient methods to isolate the targeted compounds from hydrochar are needed to pave the way for the proposed valorization routes, results in this study represent new contributions that can be used as basis for redesigning process sequences related to reutilization of HTL byproducts in wet biomass waste biorefineries.

Author contributions

H. S.: conceptualization, methodology, formal analysis, investigation, data curation, visualization, and writing – original draft. J. W. T.: conceptualization, writing – review and editing, research supervision, and funding acquisition.

Conflicts of interest

The authors declare that they have no competing financial interest.

Acknowledgements

This study was funded in part by the U.S. Department of Energy through their RAPID program with award number DE-EE0007888-9.7, the USDA grant 2019-69012-29905 involving collaborative research between Cornell University and the University of Arkansas, and the Graduate School at Cornell. This study also used the Cornell Center for Materials Research (NSF MRSEC DMR-1719875) shared facilities. H. S. also thanks the Fulbright-DIKTI Foundation for financial support as a doctoral candidate in chemical engineering at Cornell University. We also thank other research teams at Cornell including Prof. Jillian Goldfarb, Prof. Fengqi You, Dr Kui Wang, and Dr Matteo Pecchi as our discussion partners.

References

1 E. Angouria-Tsorochidou, M. Seghetta, A. Trémier and M. Thomsen, *Sci. Total Environ.*, 2022, **815**, 1–10.
2 H. Sudibyo, M. Pecchi and J. W. Tester, *Sustainable Energy Fuels*, 2022, **6**, 2314–2329.
3 H. Sudibyo, M. Pecchi, H. Harwood, M. Khare, S. Karunwi, G. Tan and J. W. Tester, *Ind. Eng. Chem. Res.*, 2022, **61**, 6894–6908.
4 U. Rao, R. Posmanik, L. E. Hatch, J. W. Tester, S. L. Walker, K. C. Barsanti and D. Jassby, *Bioresour. Technol.*, 2018, **267**, 408–415.

5 B. Wang, Z. Zhou, D. Xu, J. Wu, X. Yang, Z. Zhang and Z. Yan, *Miner. Eng.*, 2022, **181**, 107548.
6 K. Wang, Q. Ma, M. Burns, H. Sudibyo, D. L. Sills, J. L. Goldfarb and J. W. Tester, *J. Supercrit. Fluids*, 2020, **164**, 104887.
7 C. Gai, Y. Zhang, W. T. Chen, P. Zhang and Y. Dong, *RSC Adv.*, 2014, **4**, 16958–16967.
8 H. Sudibyo, K. Wang and J. W. Tester, *ACS Sustainable Chem. Eng.*, 2021, **9**, 11403–11415.
9 M. Carmona-Cabello, J. Sáez-Bastante, M. Barbanera, F. Cotana, S. Pinzi and M. P. Dorado, *Fuel*, 2022, **313**, 1–13.
10 J. Yang, Q. S. He, K. Corscadden, H. Niu, J. Lin and T. Astatkie, *Appl. Energy*, 2019, **233–234**, 906–915.
11 M. Déniel, G. Haarlemmer, A. Roubaud, E. Weiss-Hortala and J. Fages, *Waste Biomass Valorization*, 2017, **8**, 2087–2107.
12 Y. Gao, B. Yu, S. Xin, T. Mi, Y. Chen, Q. Yuan, L. Yang and P. Li, *BioResources*, 2016, **11**, 4899–4920.
13 J. Fang, L. Zhan, Y. S. Ok and B. Gao, *J. Ind. Eng. Chem.*, 2018, **57**, 15–21.
14 M. Cavali, N. Libardi Junior, R. d. A. Mohedano, P. Belli Filho, R. H. R. da Costa and A. B. de Castilhos Junior, *Sci. Total Environ.*, 2022, **822**, 153614.
15 S. A. Nicolae, H. Au, P. Modugno, H. Luo, A. E. Szego, M. Qiao, L. Li, W. Yin, H. J. Heeres, N. Berge and M. M. Titirici, *Green Chem.*, 2020, **22**, 4747–4800.
16 L. Ding, B. Zou, Y. Li, H. Liu, Z. Wang, C. Zhao, Y. Su and Y. Guo, *Colloids Surf., A*, 2013, **423**, 104–111.
17 S. Jing, Y. Zhao, R. C. Sun, L. Zhong and X. Peng, *ACS Sustainable Chem. Eng.*, 2019, **7**, 7833–7843.
18 Y. Fan, U. Hornung, K. Raffelt and N. Dahmen, *J. Anal. Appl. Pyrolysis*, 2020, **147**, 104798.
19 F. Obeid, T. C. Van, B. Guo, N. C. Surawski, U. Hornung, R. J. Brown, J. A. Ramirez, S. R. Thomas-Hall, E. Stephens, B. Hankamer and T. Rainey, *Biomass Bioenergy*, 2021, **151**, 106119.
20 B. M. Ghanim, W. Kwapinski and J. J. Leahy, *ACS Sustainable Chem. Eng.*, 2018, **6**, 11265–11272.
21 J. Lu, H. Li, Y. Zhang and Z. Liu, *ACS Sustainable Chem. Eng.*, 2018, **6**, 13570–13578.
22 American Society for Testing and Materials, *ASTM D5373-21 Standard Test Methods for Determination of Carbon, Hydrogen and Nitrogen in Analysis Samples of Coal and Carbon in Analysis Samples of Coal and Coke*, West Conshohocken, PA, United States, 2021.
23 N. Liu, U. Jørgensen and P. E. Lærke, *Energy Fuels*, 2013, **27**, 7485–7488.
24 M. Wilk, M. Śliz and M. Gajek, *Renewable Energy*, 2021, **177**, 216–228.
25 G. Tondl, C. Hammerl, C. Pfeifer and D. Pum, *Ind. Eng. Chem. Res.*, 2020, **59**, 1829–1835.
26 Z. Huang, L. Shi, Y. Muhammad and L. Li, *J. Colloid Interface Sci.*, 2021, **586**, 423–432.
27 X. Cao, K. S. Ro, M. Chappell, Y. Li and J. Mao, *Energy Fuels*, 2011, **25**, 388–397.
28 Y. Jiang, C. Ren, H. Guo, M. Guo and W. Li, *Environ. Sci. Technol.*, 2019, **53**, 13841–13849.
29 C. Falco, F. P. Caballero, F. Babonneau, C. Gervais, G. Laurent, M.-M. Titirici and N. Baccile, *Langmuir*, 2011, **27**, 14460–14471.
30 J. A. Kaduk, S. J. L. Billinge, R. E. Dinnebier, N. Henderson, I. Madsen, R. Cerny, M. Leoni, L. Lutterotti, S. Thakral and D. Chateigner, *Nat. Rev. Methods Primers*, 2021, **1**, 1–22.
31 Z. Xu, X. Ma, J. Liao, S. M. Osman, S. Wu and R. Luque, *ACS Sustainable Chem. Eng.*, 2022, **10**, 4258–4268.
32 S. Gates-Rector and T. Blanton, *Powder Diffr.*, 2019, **34**, 352–360.
33 X. Zhou, D. Liu, H. Bu, L. Deng, H. Liu, P. Yuan, P. Du and H. Song, *Solid Earth Sci. Libr.*, 2018, **3**, 16–29.
34 M. Llaver, E. F. Fiorentini, M. N. Oviedo, P. Y. Quintas and R. G. Wuilloud, *Int. J. Environ. Res. Public Health*, 2021, **18**, 1–27.
35 J. Wolff, D. Hofmann, M. Koch, R. Bol, A. Schnepf and W. Amelung, *Sci. Rep.*, 2020, **10**, 1–11.
36 J. Schellekens, P. Buurman, K. Kalbitz, A. Van Zomeren, P. Vidal-Torrado, C. Cerli and R. N. J. Comans, *Environ. Sci. Technol.*, 2017, **51**, 1330–1339.
37 B. Ashourirad, M. Demir, R. A. Smith, R. B. Gupta and H. M. El-Kaderi, *RSC Adv.*, 2018, **8**, 12300–12309.
38 M. Jerigová, M. Odziomek and N. López-Salas, *ACS Omega*, 2022, **7**, 11544–11554.
39 N. Shi, Q. Liu, X. He, G. Wang, N. Chen, J. Peng and L. Ma, *Energy Fuels*, 2019, **33**, 9904–9915.
40 M. R. Sturgeon, S. Kim, K. Lawrence, R. S. Paton, S. C. Chmely, M. Nimlos, T. D. Foust and G. T. Beckham, *ACS Sustainable Chem. Eng.*, 2014, **2**, 472–485.
41 W. Schutyser, T. Renders, S. Van Den Bosch, S. F. Koelewijn, G. T. Beckham and B. F. Sels, *Chem. Soc. Rev.*, 2018, **47**, 852–908.
42 L. Leng, L. Yang, S. Leng, W. Zhang, Y. Zhou, H. Peng, H. Li, Y. Hu, S. Jiang and H. Li, *Sci. Total Environ.*, 2021, **756**, 143679.
43 Y. Deng, T. Zhang, J. Clark, T. Aminabhavi, A. Kruse, D. C. W. Tsang, B. K. Sharma, F. Zhang and H. Ren, *Green Chem.*, 2020, **22**, 5628–5638.
44 Q. Wang, H. Jung, B. Wan, P. Liu, P. Yang and Y. Tang, *ACS Sustainable Chem. Eng.*, 2021, **9**, 10630–10641.
45 R. Huang and Y. Tang, *Environ. Sci. Technol.*, 2015, **49**, 14466–14474.
46 H. Zhang, W. Wang, L. Yuan, Z. Wei, H. Zhang and W. Zhang, *Mater. Charact.*, 2022, **187**, 111854.
47 W. Dong, C. Gilmore, G. Barr, C. Dallman, N. Feeder and S. Terry, *J. Pharm. Sci.*, 2008, **97**, 2260–2276.
48 R. Nkoa, *Agron. Sustainable Dev.*, 2014, **34**, 473–492.
49 K. Risberg, H. Cederlund, M. Pell, V. Arthurson and A. Schnürer, *J. Waste Manag.*, 2017, **61**, 529–538.
50 R. Huang, C. Fang, X. Lu, R. Jiang and Y. Tang, *Environ. Sci. Technol.*, 2017, **51**, 10284–10298.
51 American Public Health Association, *Standard Methods for the Examination of Water and Wastewater*, APHA (American Public Health Association), Washington D.C., 23rd edn, 2017.
52 R. W. Wells, *Am. J. Clin. Pathol.*, 1948, **18**, 576–578.
53 M. F. Ryan and H. Barbour, *Ann. Clin. Biochem.*, 1998, **35**, 449–459.

54 J. Bergmann, T. Monecke and R. Kleeberg, *J. Appl. Crystallogr.*, 2001, **34**, 16–19.
55 P. Sannigrahi and E. Ingall, *Geochem. Trans.*, 2005, **6**, 52–59.
56 D. Laurencin, C. Gervais, H. Stork, S. Krämer, D. Massiot and F. Fayon, *J. Phys. Chem. C*, 2012, **116**, 19984–19995.
57 J. Xu, P. Zhu, Z. Gan, N. Sahar, M. Tecklenburg, M. D. Morris, D. H. Kohn and A. Ramamoorthy, *J. Am. Chem. Soc.*, 2010, **132**, 11504–11509.
58 J. L. Andersen, C. Flamm, D. Merkle and P. F. Stadler, *IEEE/ACM Trans. Comput. Biol. Bioinf.*, 2019, **16**, 510–523.
59 M. E. Beber, M. G. Gollub, D. Mozaffari, K. M. Shebek, A. I. Flamholz, R. Milo and E. Noor, *Nucleic Acids Res.*, 2022, **50**, D603–D609.
60 T. Kahl, K. W. Schröder, F. Lawrence, W. Marshall, H. Höke and R. Jäckh, in *Ullmann's Encyclopedia of Industrial Chemistry*, ed. B. E. C. Ley, Wiley-VCH Verlag GmbH, Weinheim, Germany, 2012, pp. 45– 478.
61 R. Singh, K. Veeramani, R. Bajpai and A. Kumar, *Ind. Eng. Chem. Res.*, 2019, **58**, 5864–5872.
62 J. F. Norris, in *Experimental Organic Chemistry*, ed. F. E. Clark, McGraw-Hill, New York, 2nd edn, 1924, pp. 179–186.
63 H. Meyer, Process for the Preparation of Hydroxyphenylacetonitriles, *US Pat.*, 3983160, 1976, pp. 1–4.
64 F. Wang, J. B. Gerken, D. M. Bates, Y. J. Kim and S. S. Stahl, *J. Am. Chem. Soc.*, 2020, **142**, 12349–12356.
65 American Society for Testing and Materials, *ASTM D1385 Standard Test Method for Hydrazine in Water*, West Conshohocken, Pennsylvania, 2018.
66 Z. Qiu, L. Lv, J. Li, C. C. Li and C. J. Li, *Chem. Sci.*, 2019, **10**, 4775–4781.
67 J. N. McPherson, B. Das and S. B. Colbran, *Coord. Chem. Rev.*, 2018, **375**, 285–332.
68 S. Ramesh, P. N. Arunachalam and A. Lalitha, *RSC Adv.*, 2013, **3**, 8666–8669.
69 Z. Sepehr, H. Nasr-Isfahani, A. R. Mahdavian and A. H. Amin, *J. Iran. Chem. Soc.*, 2021, **18**, 3061–3067.
70 I. Owsik and B. Kolarz, *J. Mol. Catal. A: Chem.*, 2002, **178**, 63–71.
71 C. Hardacre, P. Nancarrow, D. W. Rooney and J. M. Thompson, *Org. Process Res. Dev.*, 2008, **12**, 1156–1163.
72 G. S. Baviera and P. M. Donate, *Beilstein J. Org. Chem.*, 2021, **17**, 2028.
73 J. N. McPherson, B. Das and S. B. Colbran, *Coord. Chem. Rev.*, 2018, **375**, 285–332.
74 J. J. Lee, in *Name Reactions*, Springer, 2014, pp. 255–256.
75 G. A. Gonçalves and V. L. Eifler-Lima, *Chem. Heterocycl. Compd.*, 2021, **57**, 734–736.
76 M. M. Abdou, *Arabian J. Chem.*, 2017, **10**, S3664–S3675.
77 A. Brahmia, T. Ben Ayed and R. Ben Hassen, *Acta Crystallogr., Sect. E: Struct. Rep. Online*, 2013, **69**, 1–6.
78 H. Fakhraian and Y. Nafari, *J. Chem. Sci.*, 2021, **133**, 1–11.
79 B. Saranya and M. Gowri, *J. Mol. Struct.*, 2022, **1250**, 131674.
80 P. Zhang, Y. Yang, X. Zheng, W. Huang, Z. Ma and Z. Shen, *Chem. Pharm. Bull.*, 2012, **60**, 270–274.
81 J. Lee, S. P. Khanapure, H. O. Kim, R. S. B. Rajur, B. Li, J. D. Williams, R. Pai and N. P. Peet, *Synth. Commun.*, 2010, **40**, 3390–3396.
82 X. Fu, Y. Liao, C. R. Glein, M. Jamison, K. Hayes, J. Zaporski and Z. Yang, *ACS Earth Space Chem.*, 2020, **4**, 722–729.
83 A. S. Tikhomirov, I. V. Ivanov, A. M. Korolev and A. E. Shchekotikhin, *Tetrahedron*, 2019, **75**, 130623.
84 Z. Wang and H. Qin, *Chem. Commun.*, 2003, **2**, 2450–2451.
85 C. G. Neochoritis, T. Zhao and A. Dömling, *Chem. Rev.*, 2019, **119**, 1970–2042.
86 V. Amarnath, D. C. Anthony, K. Amarnath, W. M. Valentine, L. A. Wetterau and D. G. Graham, *J. Org. Chem.*, 1991, **56**, 6924–6931.
87 T. Shen, R. Hu, C. Zhu, M. Li, W. Zhuang, C. Tang and H. Ying, *RSC Adv.*, 2018, **8**, 37993–38001.
88 H. Orzales, 3-(4'-Alkoxy-Benzoyl)-1,2,2-Trimethyl-Cyclopentane-Carboxylicacids, Their Optical Isomers And Drugs Containing Such Compounds, *US Pat.*, 4113960, 1978, pp. 1–5.
89 S. Bagchi, A. Monga, S. Kumar, D. Deeksha and A. Sharma, *ChemistrySelect*, 2018, **3**, 12830–12835.
90 X. Xiong, C. Yi, X. Liao and S. Lai, *Catal. Lett.*, 2019, **149**, 1690–1700.
91 E. Dolci, V. Froidevaux, C. Joly-Duhamel, R. Auvergne, B. Boutevin and S. Caillol, *Polym. Rev.*, 2016, **56**, 512–556.
92 E. Arceo, J. A. Ellman and R. G. Bergman, *ChemSusChem*, 2010, **3**, 811–813.
93 P. N. Nelson, *J. Mol. Struct.*, 2019, **1181**, 423–427.
94 M. N. Lund and C. A. Ray, *J. Agric. Food Chem.*, 2017, **65**, 4537–4552.
95 D. Lisicki, K. Nowak and B. Orlińska, *Materials*, 2022, **15**, 1–14.
96 K. Godula, B. Sezen and D. Sames, *J. Am. Chem. Soc.*, 2005, **127**, 3648–3649.
97 X. F. Xu, S. Zilberg and Y. Haas, *J. Phys. Chem. A*, 2010, **114**, 4924–4933.
98 B. F. Abdel-Wahab, R. E. Khidre and A. A. Farahat, *Arkivoc*, 2011, **2011**, 196–245.
99 J. Richard, J. Joseph, C. Wang, A. Ciesielski, J. Weiss, P. Samorì, V. Mamane and J. A. Wytko, *J. Org. Chem.*, 2021, **86**, 3356–3366.
100 R. M. Tikhov and N. Y. Kuznetsov, *Org. Biomol. Chem.*, 2020, **18**, 2793–2812.
101 Z. Wang and H. Qin, *Chem. Commun.*, 2003, **2**, 2450–2451.
102 H. A. Höppe, *Z. Anorg. Allg. Chem.*, 2005, **631**, 1272–1276.
103 M. A. Pasek, J. M. Sampson and Z. Atlas, *Proc. Natl. Acad. Sci. U. S. A.*, 2014, **111**, 15468–15473.
104 E. Boanini, F. Silingardi, M. Gazzano and A. Bigi, *Cryst. Growth Des.*, 2021, **21**, 1689–1697.
105 D. Lee, C. Leroy, C. Crevant, L. Bonhomme-Coury, F. Babonneau, D. Laurencin, C. Bonhomme and G. De Paëpe, *Nat. Commun.*, 2017, **8**, 1–7.
106 H. Agougui, A. Aissa and M. Debbabi, *Appl. Surf. Sci.*, 2012, **261**, 182–188.
107 D. Bezold, T. Dürr, J. Singh and H. J. Jessen, *Chem.–Eur. J.*, 2020, **26**, 2298–2308.
108 A. M. Chaka, *ACS Earth Space Chem.*, 2018, **2**, 210–224.
109 T. Tone and N. Koga, *ACS Omega*, 2021, **6**, 13904–13914.
110 L. Pérez-Villarejo, F. Takabait, L. Mahtout, B. Carrasco-Hurtado, D. Eliche-Quesada and P. J. Sánchez-Soto, *Ceram. Int.*, 2018, **44**, 5291–5296.

